SECOND HARMONIC GENERATION FROM InGaAsP WAVEGUIDE

SECOND HARMONIC GENERATION FROM InGaAsP WAVEGUIDE AT 1.3 μm WAVELENGTH

By
ROBERT MICHAEL BIERMAN, B.Sc.

A Thesis
Submitted to the School of Graduate Studies
in Partial Fulfillment of the Requirements
for the Degree
Master of Engineering

McMaster University
Hamilton, Ontario
Canada
October, 1992

MASTER OF ENGINEERING (1992)
(Engineering Physics)

McMASTER UNIVERSITY
Hamilton, Ontario

TITLE: Second Harmonic Generation from InGaAsP Waveguide at 1.3 μm Wavelength

AUTHOR: Robert Michael Bierman, B. Sc. (University of New Brunswick)

SUPERVISORS: Dr. J.G. Simmons and Dr. D. Thompson

NUMBER OF PAGES: xi , 91

ABSTRACT

Results of research on surface emission from a waveguide due to second-harmonic generation are presented. This concept has been applied and demonstrated here in the InP-InGaAsP material system for the first time, using a fundamental wavelength of 1.32 μm and a harmonic surface emission at 660 nm. The surface emission is the result of the nonlinear mixing of two counterpropagating modes in a waveguide. The theory of nonlinear optics that produces this effect is explained, leading up to a model that describes the behaviour of the surface emitting waveguide (SEWG). This model is then used to design a pseudo-optimized structure that was subsequently grown, characterized and tested. Device performance and behaviour are compared with theoretical predictions.

ACKNOWLEDGEMENTS

This project was only possible with the aid and support of numerous people, to whom I am greatly appreciative and indebted. I am especially thankful to both Dr. Michael Cada and Dr. Mikelis Svilans for their expertise, enthusiasm and effort on this project. Many thanks for their guidance in keeping me on track when I went astray. Thanks are also extended to Dr. Sigfried Janz and Dr. Richard Normandin of the Solid State Opto-electronics Consortium at the National Research Council, Ottawa, for their invaluable input and assistance in modeling and testing of our devices. I am also grateful to my supervisors, Dr. John Simmons and Dr. David Thompson, for their wisdom and encouragement throughout this work. Hopefully I have established some healthy professional and personal relationships that will last for many years to come.

Thanks also go to the staff at Bell-Northern Research's Advanced Technology Lab for their support in growth, processing and analysis, and for providing an exciting and enjoyable work environment during my stay at BNR. Further thanks go to the Natural Science and Engineering Research Council (NSERC), the CITR, and McMaster University for financial support.

TABLE OF CONTENTS

LIST OF FIGURES

LIST OF TABLES

LIST OF SYMBOLS

A_{nl}	nonlinear cross-section
$\vec{B}$	magnetic induction
β	effective waveguide propagation constant
$\Delta\beta$	$\beta_1 - \beta_2$
c	speed of light
χ	electronic susceptibility
$\chi^{(1)}$	first-order electronic susceptibility
$\chi^{(2)}$	second-order electronic susceptibility
$\chi^{(2)}_{ijk}$, $\chi^{(2)}_{im}$	tensor form of $\chi^{(2)}$
d_{ijk}, d_{im}	$= 1/2\ \chi^{(2)}_{ijk}$
$\vec{E}$	electric field
$E_i(t)$	component of $\vec{E}$ polarized in direction represented by i
$\vec{E}_g(t)$	Green's function electric field
E_{TE}	electric field for TE-polarized waveguide mode
E_{TM}	electric field for TM-polarized waveguide mode
$\xi(t)$	normalized electric field
ε_o	permittivity of free space
ε	material permittivity
e	electronic charge
F	force
ϕ	phase angle
h	waveguide thickness
$\vec{H}$	magnetic flux
k_p, q, p	lateral waveguide propagation constants
k	optical propagation constant
λ	wavelength
λ_o	vacuum wavelength
m	mass
μ_o	permeability of free space
μ	material permeability

$n1, n2, n3$	refractive index of superstrate, guide and substrate
n_{eff}	effective index of refraction
N	atomic density
n	material index of refraction (complex)
$P_i(t)$	component of $\vec{P}_{NL}$ polarized in direction represented by i
$\vec{P}$	polarization field
P_{SH}	power of radiated second-harmonic
$\vec{P}_{NL}$	nonlinear dipole field
ρ	charge density
σ	electrical conductivity
SHG	second-harmonic generation
SH	second-harmonic
t	time variable
θ	emission angle
$V(x)$	potential energy versus position
ω, ω_i	radial frequency of light
$x(t)$	electronic position versus time
Z	impedence of free space

CHAPTER 1: INTRODUCTION

1.1 NONLINEAR OPTICS

The invention of the laser is responsible for spawning the field of Nonlinear Optics. The high intensity fields produced by the laser allowed the observation of high-order optical nonlinearities. The groundwork began as early as 1961 with the experimental work of Franken and co-workers [1] on optical second-harmonic generation. Since then, the field has expanded enormously and includes sum- and difference-frequency generation, parametric amplification and oscillation, four-wave mixing, different nonlinear spectroscopies, phase conjugation, optical bistability, optical switching, plus a host of nonlinear effects.

1.2 SECOND HARMONIC GENERATION (SHG)

Second harmonic generation is one of many effects arising in solids caused by the non-linearity of the dielectric function. The electronic response of a material to an applied electromagnetic field is described by the macroscopic polarization. The polarization is typically proportional to the field, which is manifested as the material index of refraction, but the relationship between polarization and electric field can be nonlinear. This means the polarization has components proportional to powers of the field. The first nonlinear term is proportional to the square of the applied electric field. A direct consequence of this nonlinearity is second-harmonic generation, where a part of the applied field is converted to a field at twice the frequency. The frequency-doubling properties of crystals have been studied and characterized for years and are still the subject of much current research. The main goal of such studies is to maximize the efficiency of conversion from the fundamental to the harmonic wavelength. The III-V semiconductors such as GaAs and InP make excellent candidates for this purpose, having some of the highest nonlinear susceptibilities of all solids, as shown in Table 1.1. To make optimum use of the non-linearity,

Table 1.1 : The Nonlinear Optical Susceptibilities of a Number of Crystals

Crystal	$d_{im}^{(2\omega)}$ *in units of* $\frac{1}{9}\varepsilon_o \cdot 10^{-22} MKS$		δ_{im} *in units of* 10^9
$LiIO_3$	d_{15}	= 4.4	
$NH_4H_2PO_4$	d_{36}	= 0.45	3.2
(ADP)	d_{14}	= 0.50 ± 0.02	3.2
KH_2PO_4	d_{36}	= 0.45 ± 0.03	3.4
(KDP)	d_{14}	= 0.35	3.4
KD_2PO_4	d_{36}	= 0.42 ± 0.02	3.1
	d_{14}	= 0.42 ± 0.02	3.1
Quartz	d_{11}	= 0.37 ± 0.02	2.3
$AlPO_4$	d_{11}	= 0.38 ± 0.03	2.5
ZnO	d_{33}	= 6.5 ± 0.2	4.0
	d_{31}	= 1.95 ± 0.2	1.3
	d_{15}	= 2.1 ± 0.2	1.5
CdS	d_{33}	= 28.6 ± 2	3.8
	d_{31}	= 30 ± 10	1.9
	d_{36}	= 33	2.3
GaP	d_{14}	= **80** ± 14	1.5
GaAs	d_{14}	= **72**	2.0
$BaTiO_3$	d_{33}	= 6.4 ± 0.5	1.3
	d_{13}	= 18 ± 2	3.1
	d_{15}	= 17 ± 2	2.9
$LiNbO_3$	d_{15}	= 4.4	1.4
	d_{22}	= 2.3 ± 1.0	0.66
Te	d_{11}	= 517	0.8
Se	d_{11}	= 130 ± 30	5.0

The quantity d_{im} is defined by $d_{im} = \chi_{im}/2$, where χ_{im} is the second order nonlinear susceptibility; it is a measure of the nonlinearity of a material (see Ch.2 for a discussion). The quantity δ_{im} is known as Miller's delta and is important because its value remains remarkably constant over a wide range of materials. (Reproduced from ref [2].)

most efforts employ an optically collinear scheme, where the fundamental and harmonic beams travel in the same direction, transferring energy between them. The beams must satisfy a phase matching condition to maximize energy flow to the harmonic. This means that the spatial wavelength (inside the material) at the harmonic frequency is exactly half that of the fundamental. The two waves maintain a coherent phase relationship as they propagate through the crystal. If phase matching is not achieved, then the photons transferred to the harmonic will destructively interfere, resulting in poor efficiency. In terms of wavevector, this relation appears as:

$$\mathbf{k}^{(2\omega)} = 2\cdot\mathbf{k}^{(\omega)} \tag{1.1}$$

Phase matching represents the key to efficient second-harmonic generation and is *the* central issue in maximizing output. The most successful methods use the special properties of crystals to achieve this goal, such as birefringence and ferroelectric effects.

Since the III-V semiconductor crystals common to optoelectronics possess none of these exotic properties, phase matching is not achievable. However, by utilizing a second harmonic (SH) generated beam emitted perpendicular to the fundamental, the phase matching condition is relaxed in the standard sense. This leads to surface emission from the crystal in the case of waveguide (WG) propagation.

In this scheme, the second harmonic beam propagates through the waveguide to the surface. The net output is the sum of contributions from all points in the waveguide. At any instant in time, the SH light generated in the waveguide has a coherent phase relationship along the depth of the waveguide. After propagating to the surface, the SH light interferes destructively, resulting in low output. Previous attempts [3] to capitalize on this idea demonstrated exceedingly small conversion efficiencies, as small as $\sim 1\text{x}10^{-13}$. However, a method for enhancing the conversion efficiencies [4] to as high as 10^{-5} has been realized by using a multilayer half-wave stack as the waveguide. With the promise of even higher conversion efficiencies, the surface emitting waveguide (SEWG) has drawn considerable attention for its potential as an optoelectronic and telecommunications device.

1.3 THE SURFACE EMITTING WAVEGUIDE (SEWG)

The SEWG is an all-optical solid state device consisting of a waveguide capable of emitting an optical beam from its surface. Surface emission from the waveguide is the result of the non-linear mixing of two counter-propagating optical beams of different frequencies. While the two fundamental beams propagate back and forth in the waveguide, a harmonic signal at the sum frequency is emitted from the top surface. An equivalent beam is lost to the substrate. The surface-emitted beam is coherent and carries any information from the fundamental beams.

This is effectively a 3-field mixing interaction involving the input of two fundamental fields and the output of a sum frequency field. A schematic of the process is shown in Fig. 1.1. The combining of two photons to emit a third photon at the sum frequency must obey momentum conservation. This can lead to surface emission at an angle, determined by the difference in propagation constants between the two mixing waveguide (WG) modes. This process is shown in Fig. 1.2.

The SEWG has several potential applications in optoelectronics and telecommunications. Experiments in lithium niobate waveguides were performed in the late 1970's by Normandin and Stegeman [5] but the device was first shown to have potential in the III-V semiconductors in 1990, by Normandin et al [4].

1.4 APPLICATIONS

Since device performance is based on a mixing process and preserves coherence, there are numerous applications in signal processing. Vakhshoori and Wang [6] demonstrated usage as an integrable optical correlator . Here, a short pulse is launched in the SEWG and the pulse mixes with its reflection from the far facet. An extension of this concept for picosecond signal processing has also been demonstrated by Normandin and Stegeman [7], where two different counterpropagating pulses are mixed. The resulting SH output is a convolution of the two pulses. Note that this is now sum-frequency generation, of which second harmonic generation is a special case.

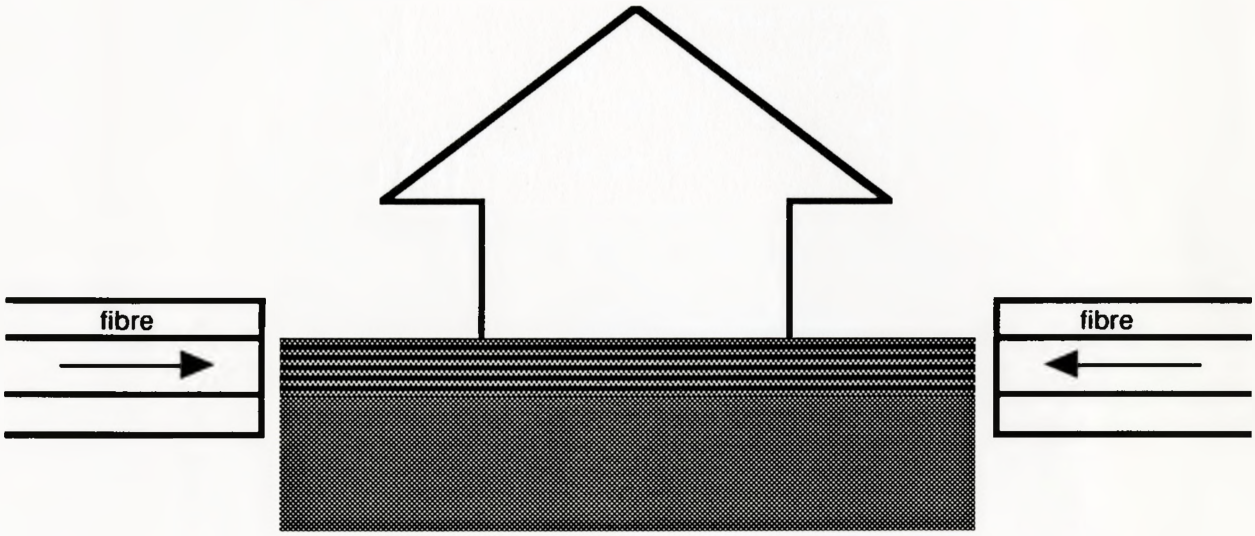

Fig. 1.1: Diagram showing coupling of light from optical fibres to a waveguide, where two counter-propagating beams mix, resulting in surface emission at the sum frequency.

Another application is as a spectrometer. The angle of surface emission of the SH signal is related to the difference in propagation constants, which are functions of wavelength. If an input signal is mixed with a second beam of known wavelength (acting as a local oscillator), the wavelength can be determined by measuring the angle of surface emission. Resolutions on the order of 1Å are achievable [8] , effectively replacing a tabletop spectrometer with a waveguide only 3-4 mm long!

The SEWG is also useful as a wavelength division demultiplexer. The principle of operation is similar to that of the spectrometer except that several information-bearing signals, each at a different wavelength, are simultaneously mixed with a local oscillator. Each signal will result in surface emission at different directions. These harmonics can be illuminated onto an array of detectors, effectively demultiplexing the different information channels.

1.5 SUMMARY OF MOTIVATION AND GOALS OF THESIS

A working model of the SEWG is given in [4,8] which describes device behaviour and predicts the conversion efficiency of the device. In order to exploit the range of possible applications for the SEWG, there are several key issues that must be addressed. The present model of conversion efficiency is only an approximation: it does not treat the phase of the harmonic signal accurately. Also, the model fails to treat the waveguide as an optically active multilayer stack. In order to aid future progress, it is important to identify and eliminate these approximations wherever necessary and to further develop the model as a whole.

Past work has only been carried out in the GaAs-AlGaAs semiconductor system. Operation in the silica fibre communication windows of 1.3 μm and 1.55 μm is desired. To monolithically integrate the SEWG with other devices operating at these wavelengths, such as lasers, it should be designed and grown in the InP-InGaAsP material system. It was with the aim of improving the current device model and exploring the feasibility of the InGaAsP system that the work presented here was undertaken.

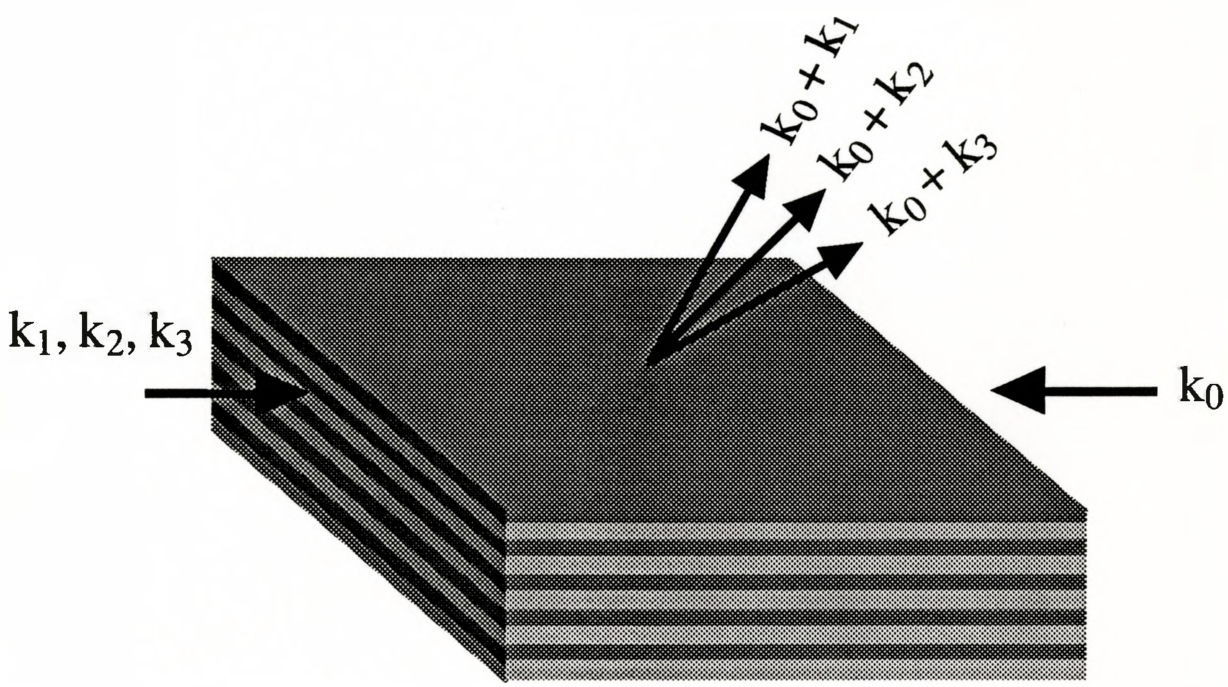

Fig. 1.2: Diagram showing frequency dependence of emission angle from the waveguide surface. The mixing process must obey momentum conservation for the incoming and outgoing beams. Note that the downward travelling beam is lost to the substrate (not shown).

Chapter 2 of this thesis gives an overview of nonlinear crystal theory and a general explanation of the origins of second harmonic generation. A model of the SEWG device is developed in Chapter 3, including a derivation of SH conversion efficiency. In Chapter 4 the design for an InP-based SEWG is described, based on simulations calculated with a computer algorithm. The physical parameters of the device - complex index of refraction and nonlinear susceptibility - and their effects on device performance are also discussed. In Chapter 5, the growth and characterization of the structure is described. A discussion of the experimental apparatus and results is given in Chapter 6. The conclusion, Chapter 7, contains a brief summary and suggests possible avenues to improve and extend this work.

CHAPTER 2 - NONLINEAR OPTICS AND TENSOR ANALYSIS

This chapter describes the physical origins of nonlinear optics (NLO), concentrating on the phenomenon of second harmonic generation. It will also discuss the tensorial representation of SHG, using the relevant crystal class of zincblende as an example. The theory of nonlinear optics was laid down in the 1960's when the laser gained popularity as a tool for experimentation. There are several recent reviews of nonlinear optics available but they invariably refer to the original papers quoted in this work.

2.1 MAXWELL'S EQUATIONS

The basis of NLO arises from the nonlinear response of materials to an applied electromagnetic field. Maxwell's equations, which govern electromagnetic processes, are perfectly linear equations:

$$\vec{\nabla} \cdot \vec{H} = 0 \tag{2.1}$$

$$\vec{\nabla} \cdot \vec{D} = -\rho \tag{2.2}$$

$$\vec{\nabla} \times \vec{E} = -\frac{\partial \vec{B}}{\partial t} \tag{2.3}$$

$$\vec{\nabla} \times \vec{H} = \frac{\partial \vec{D}}{\partial t} \tag{2.4}$$

However, it is the constitutive equations based on material properties connecting charge and current distributions to the EM fields that are, in general, nonlinear:

$$\vec{D} = \varepsilon_o \vec{E} + \vec{P} = \varepsilon_o \left[1 + \chi^{(1)} + \chi^{(2)}\vec{E} + \chi^{(3)}\vec{E}^{\,2} + \ldots\right]\vec{E} \tag{2.5}$$

$$\vec{J} = \left[\sigma^{(1)} + \sigma^{(2)}\vec{E} + \ldots\right] \vec{E} \tag{2.6}$$

$$\vec{B} = \left[\mu^{(1)} + \mu^{(2)}\vec{H} + ...\right] \vec{H} \tag{2.7}$$

Higher order terms are generally ignored, leaving a completely linear theory of Optics. When the nonlinear terms of the constitutive equations are included, a host of phenomena are revealed.

One consequence of a nonlinearity in (2.5) is an energy exchange between EM fields at different frequencies. The nonlinear dielectric response of a crystal produces a polarization proportional to the square of the electric field (and possibly higher order terms as well). This polarization radiates, resulting in second harmonic generation where part of an EM wave propagating through a crystal at frequency ω is converted to a wave propagating at frequency 2ω.

2.2 A PHYSICAL INTERPRETATION OF OPTICAL NONLINEARITY

2.2.1 Classical Anharmonic Oscillator Model

The classical anharmonic oscillator model can be used to give a fundamental understanding of SHG. The loosely bound valence electrons are known to be the dominant contributors to optical polarization [9]. An expression for the polarization, p(t), of an electron is given by,

$$p(t) = -e\, N\, x(t) \tag{2.8}$$

where N is the density of atoms per unit volume, e is the electronic charge and x(t) is the electronic displacement from equilibrium. Following the argument of Yariv [10], the potential energy V(x) of a symmetric crystal must reflect the crystal symmetry, so that

$$V(x) = \frac{m}{2}\omega_0^2 x^2 + \frac{m}{4} B x^4 + ... \tag{2.9}$$

where ω_0, B, and m are constants. Note that V(x) can only possess even powers of x, which satisfies the symmetry condition V(x) = V(-x). The force required to displace an electron is:

$$F = -\frac{\partial V}{\partial x} = -m\,\omega_0^2\,x - m\,B\,x^3 \qquad (2.10)$$

The linear polarization (which gives rise to index of refraction) is caused by the first term of (2.10). Next, consider the shape of the symmetric potential well V(x). The electronic displacement will be symmetric around x=0, even though higher order terms are present.

If the crystal is asymmetrical then odd powers of x may appear in the potential:

$$V(x) = \frac{m}{2}\,\omega_0^2\,x^2 + \frac{m}{3}\,D\,x^3 + \ldots \qquad (2.11)$$

Graphs of the potential for both the symmetric and asymmetric case are shown in Figure 2.1. The resulting restoring force is given by,

$$F = -\frac{\partial V}{\partial x} = -(m\,\omega_0^2\,x + m\,B\,x^2) \qquad (2.12)$$

To see how this result leads to a nonlinear system response, consider an asymmetrical crystal in an electric field at frequency $\omega << \omega_0$. A plot of the electronic displacement versus applied electric field is also shown in Figure 2.1. It is clear that for positive (E>0) electric fields, the electronic displacement will be smaller than for negative fields of equal magnitude (i.e. stiffer restoring force). As the electron oscillates in the electric field, the excursions from equilibrium will be smaller for positive displacements than for negative ones. This is shown in Figure 2.2, which is a graph of p(t) versus time.

A Fourier analysis of this motion shows three terms (Fig. 2.3): a fundamental term, a harmonic term and a dc rectification term (plus higher order terms). It is this harmonic term that produces SHG from the radiating electronic dipole. In constrast, a similar Fourier analysis of the symmetric case shows no second harmonic term at all.

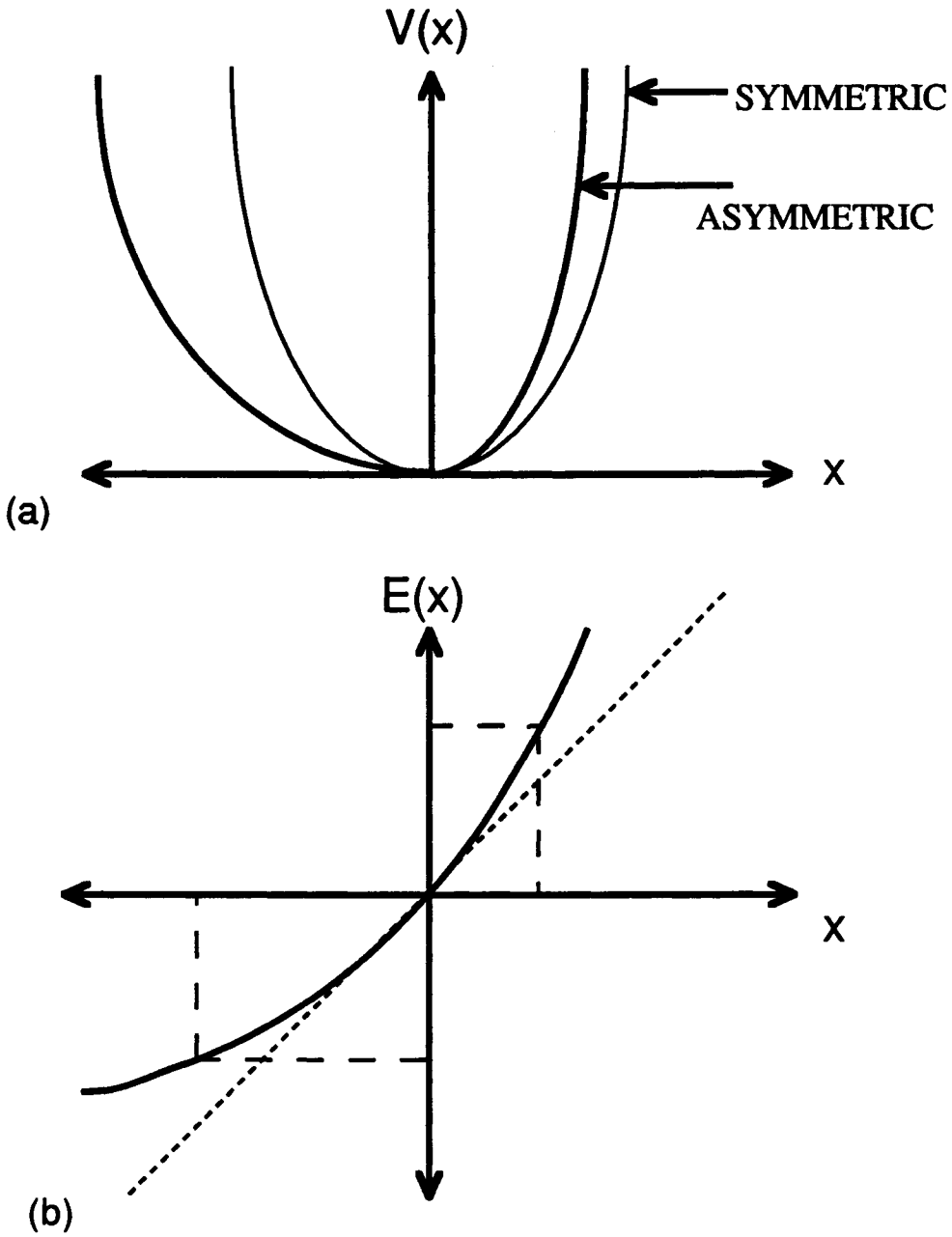

Fig. 2.1: (a) Potential energy wells for outer valence electron of crystalline solid for both symmetric and asymmetric cases. (b) 1-dimensional graph of electronic displacement, x, as a function of applied electric field E(x) for the asymmetric case. The displacement of the electron for a positive electric field is smaller than for a negative electric field. The dashed line represents the linear case. Note that for small electric fields, the response is approximately linear.

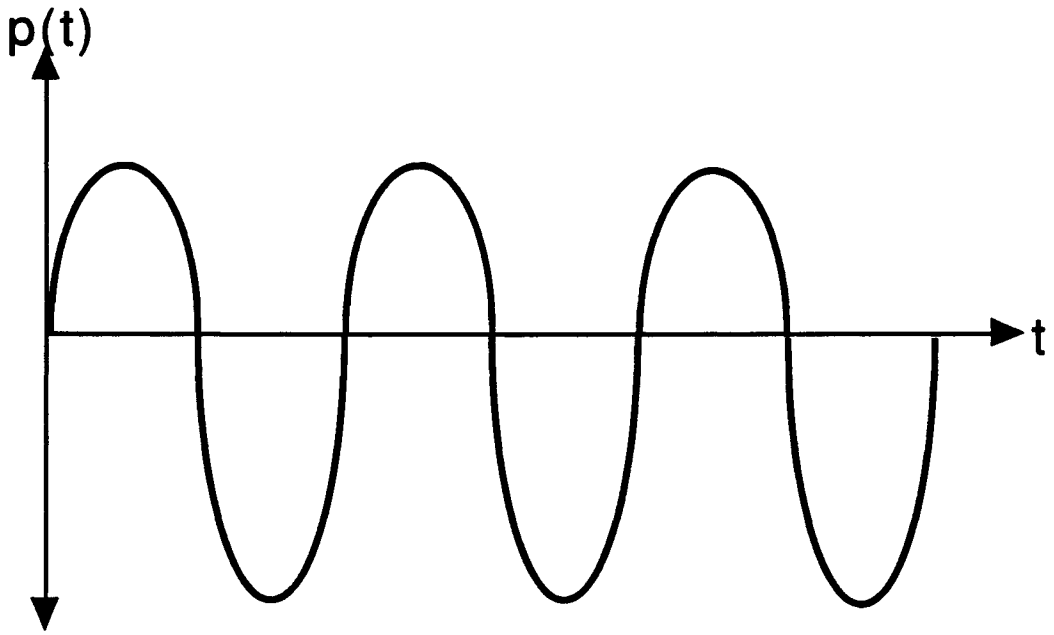

Fig. 2.2: Plot of electronic polarization versus time. When the electron's displacement is negative, the effective amount of travel is greater. This results in larger polarization in the negative direction, yielding nonlinear electronic motion which produces second-harmonic generation from the radiating dipole.

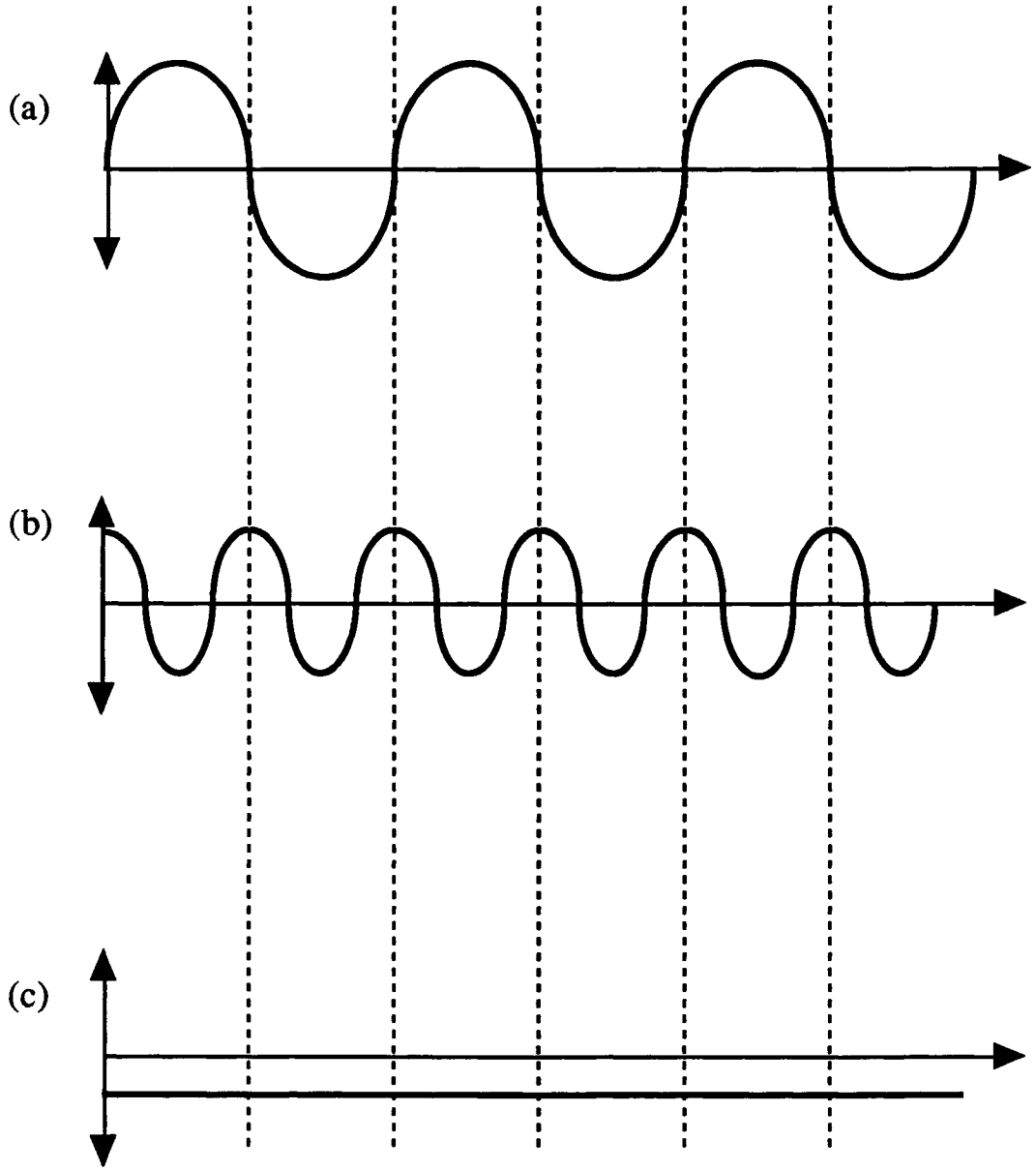

Fig. 2.3: A Fourier decomposition of the electronic polarization, showing (a) the fundamental frequency, (b) the harmonic frequency, and (c) DC rectification.

This has established the requirement that a crystal with inversion symmetry (i.e. V(x) = V(-x)) cannot possess a second order nonlinearity.

2.2.2 Nonlinear Susceptibility, $\chi^{(2)}$

It is possible to relate the nonlinear polarization to the driving field. In general this is done by writing the polarization as an expansion of powers of the electric field which appears in a simplified form as:

$$\vec{P} = \varepsilon_o [\, \chi^{(1)} + \chi^{(2)}\vec{E} + \chi^{(3)}\vec{E}^{\,2} + ...] \vec{E} \qquad (2.13)$$

where $\chi^{(n)}$ is the nth order susceptibility. In this work, we are interested in the consequences of the second order susceptibility but there are still a host of effects arising from the higher order terms. The third order susceptibility, for example, is responsible for stimulated Raman scattering [11], the DC electro-optic Kerr effect [11], intensity-dependent index of refraction effect.

The second order nonlinearity is given in a simplified form by:

$$\vec{P} = \varepsilon_o \chi^{(2)} \vec{E} \cdot \vec{E} \qquad (2.14)$$

where the exact nature of the multiplication of the fields has been omitted. Taking an applied field composed of two plane waves travelling in opposite directions with different frequencies,

$$E = E_1 \cos(\omega_1 t - k_1 x) + E_2 \cos(\omega_2 t + k_2 x) \qquad (2.15)$$

we can calculate the resultant nonlinear polarization by substituting (2.15) into (2.14) to find,

$$P = \frac{1}{2}\varepsilon_o \chi^{(2)}E_1^2 \left[1 + \cos(2\omega_1 t - 2k_1 x)\right]$$
$$+\frac{1}{2}\varepsilon_o \chi^{(2)}E_2^2 \left[1 + \cos(2\omega_2 t + 2k_2 x)\right]$$
$$+ \varepsilon_o \chi^{(2)}E_1E_2 \left[\cos(\{\omega_1+\omega_2\}t - \{k_1-k_2\}x) + \cos(\{\omega_1-\omega_2\}t - \{k_1+k_2\}x)\right]$$

(2.16)

The first two terms describe both DC rectification and SHG, while the 3rd term describes sum and difference frequency generation. Note that the spatial periodicity of the sum frequency term depends on the difference in propagation constants while the difference frequency term depends on the sum. Some or all of these effects will occur when two fields interact (cases where some of these effects cannot occur will become evident later). Note that SHG and DC rectification are simply special cases of sum and difference frequency generation where $\omega_1 = \omega_2$.

2.3 TENSORIAL FORM OF NONLINEAR SUSCEPTIBILITY

The above analysis ignored the tensorial nature of the susceptibility. The proper form for the relation between polarization and electric field is,

$$P_i(t) = \varepsilon_o \sum_{jk} \chi^{(2)}_{ijk} E_j(t) E_k(t) \qquad (2.17)$$

where the indices {i,j,k} are ranged over the coordinates {x,y,z}. The 2nd order nonlinear susceptibility is a 3rd rank tensor, meaning it is similar in form to a 3x3x3 matrix with 27 components.

It is more appropriate to phrase the relation (2.17) in terms of the frequency components of the field. The Fourier components of a field may be defined by,

$$U(t) = \frac{1}{2}\left[U(\omega)e^{i(\vec{k}\cdot\vec{r} - \omega t)} + \text{c.c.} \right] \qquad (2.18)$$

Now, let's assume that there are two fields incident on a nonlinear medium, field E_j at frequency ω_2 and field E_k at frequency ω_1. Substituting for the polarization and fields using (2.18) into (2.17), we find the polarization Fourier component at the sum frequency is given by,

$$P_i(-\omega_3) = \frac{\varepsilon_0}{2} \sum_{jk} \chi^{(2)}_{ijk}(-\omega_3,\omega_2,\omega_1)\, E_j(\omega_2)\, E_k(\omega_1) \exp i[(\vec{k}_2+\vec{k}_1-\vec{k}_3)\cdot\vec{r}] \qquad (2.19)$$

where we have made the substitution $\omega_3 = \omega_1 + \omega_2$, and ω_1 and ω_2 are the fundamental field frequencies and ω_3 is the harmonic frequency. (A similar term for the difference frequency polarization can also be found.) The three interacting fields are paired with the tensor indices by (ω_3: i), (ω_2: j), (ω_3: k). The value of the index is determined by the polarization direction of the field it is paired with. Note that the negative sign accompanying the ω_3 term is a mathematical remnant and has no physical significance.

2.4 CRYSTAL SYMMETRY

Crystal symmetry is a powerful tool in studying the physical properties of crystals. Neumann's principle is accepted as the basis for studying the effects of symmetry. Neumann's principle states that, "every physical property of a crystal must possess at least the symmetry of the point group of the crystal" [12]. The point group of a crystal is different from the space group of the crystal - it describes the symmetry operations under which the lattice is invariant, such as reflection, inversion and rotation.

The linear susceptibility $\chi^{(1)}$ displays the symmetry properties of the crystal medium, as exemplified by birefringence in certain materials. Similarly, the second order nonlinear susceptibility must also display these properties. The first consequence of this fact is that $\chi^{(2)}$ must be zero in centrosymmetric materials (a crystal that possesses inversion symmetry).

This can be understood by considering the following argument. Let us reverse the electric field applied to a centrosymmetric medium i.e. $E_j(t) \rightarrow -E_j(t)$ and $E_k(t) \rightarrow -E_k(t)$. The field would "see" a lattice that is unchanged because of its symmetry. This means the polarization must maintain its relationship to the electric field, so it must change sign as

well i.e. $P_i(t) \rightarrow - P_i(t)$. These quantities can now be substituted into (2.19) to yield the following equation:

$$- P_i(t) = \varepsilon_o \sum_{jk} \chi^{(2)}_{ijk} \left(-E_j(t)\right)\left(-E_k(t)\right) \qquad (2.20)$$

Equations (2.17) and (2.20) can simultaneously be valid only if $\chi^{(2)}$ is zero. Hence the second order nonlinear optical effects are limited to non-centrosymmetric media.

A further symmetry relation [13,14] states that for a lossless medium $\chi^{(2)}(\omega_3,\omega_2,\omega_1)$ is invariant under any permutation of the 3 pairs $(-\omega_3,i)$, (ω_2,j), (ω_1,k). Kleinman conjectured another symmetry relation [15] that states the permutation of the frequencies is irrelevant in a lossless medium. Thus $\chi^{(2)}$ is symmetric under any permutation of its indices (i,j,k). This means that the susceptibility is the same for all interactions involving the same frequencies, including sum and difference frequency generation, making computation much simpler.

2.5 TENSOR NOTATION

It is more common to express the nonlinear susceptibility in terms of the tensor $d^{(2)}$ defined by

$$d^{(2)}_{ijk} = \frac{1}{2} \chi^{(2)}_{ijk} \qquad (2.21)$$

which simplifies (2.21) to

$$P_i(-\omega_3) = \varepsilon_o \, d^{(2)}_{ijk}(-\omega_3,\omega_2,\omega_1) \;\; E_j(\omega_2) \, E_k(\omega_1) \exp i\left[(\vec{k}_2+\vec{k}_1-\vec{k}_3)\cdot\vec{r}\right] \qquad (2.22)$$

where the summation across j,k is implicit (following the Einstein summation convention). The use of $d^{(2)}$ eliminates a factor of 2 from the equations and is simply easier to write.

Kleinman symmetry states that any permutation of the indices will have no effect on the value of the component e.g. $d_{123} = d_{132} = d_{312} = d_{321}$. It is not only cumbersome to list the components of the 3x3x3 tensor, it is redundant. Therefore, we define a reduced

notation that allows us to simplify the form of the tensor. The accepted convention is chosen so that a single index m replaces the two indices (jk) using the correspondence

(jk):	11	22	33	23,32	31,13	21,12
	↓	↓	↓	↓	↓	↓
m :	1	2	3	4	5	6

Instead of having a 3x3x3 tensor with 27 components, it is possible to write d_{im} as a 3x6 tensor with only 18 components. In expanded tensor notation, (2.24) appears as

$$\begin{bmatrix} P_x \\ P_y \\ P_z \end{bmatrix} = \varepsilon_o \begin{bmatrix} d_{11} & d_{12} & d_{13} & d_{14} & d_{15} & d_{16} \\ d_{21} & d_{22} & d_{23} & d_{24} & d_{25} & d_{26} \\ d_{31} & d_{32} & d_{33} & d_{34} & d_{35} & d_{36} \end{bmatrix} \begin{bmatrix} E_x^2 \\ E_y^2 \\ E_z^2 \\ 2E_yE_z \\ 2E_xE_z \\ 2E_xE_y \end{bmatrix} e^{i(\vec{k}_1+\vec{k}_2-\vec{k}_3)\cdot\vec{r}} \tag{2.23}$$

2.6 III-V SEMICONDUCTOR POINT GROUP

The simplest crystal class with non-zero $\chi^{(2)}$ is the $\bar{4}3m$ point group [16], which includes the tetrahedrally arranged solids of the III-V, II-VI and IV families. The symmetry operations making up this group are: { E, $8C_3$, $3C_2$, 6σ, $6S_4$ }. E represents the identity operation; $8C_3$ means 8 possible rotations by 120°; $3C_2$ means 3 possible rotations of 180°; 6σ means 6 possible plane reflections; and $6S_4$ means 6 possible rotations of 90° followed by a reflection through the plane normal to the rotation axis.

These symmetry operations reduce the number of non-zero components of the susceptibility tensor in a way similar to the argument given for inversion symmetry. The principle behind using symmetry is an equivalence between the transformation of a tensor component d_{ijk} and the coordinates ijk. For example consider the effect of the C_2 rotation that transforms the coordinates (x, y, z) to (-x, -y, z). Now, the tensor component d_{xxy} transforms as xxy. After the transformation this becomes -xxy. By Neumann's principle we require the two results to be equal which leads immediately to the result that $d_{xxy} = -d_{xxy} = 0$. Overall, the 180° rotations lead to the following results:

$$\chi^{(2)}_{iii} = - \chi^{(2)}_{iii} = 0 \tag{2.24a}$$

$$\chi^{(2)}_{iij} = - \chi^{(2)}_{iij} = 0 \tag{2.24b}$$

$$\chi^{(2)}_{ijj} = - \chi^{(2)}_{ijj} = 0 \tag{2.24c}$$

Similarly, the mirror reflections provide the result that

$$\chi^{(2)}_{ijk} \; (\; i \neq j \neq k \;) \text{ invariant under permutation of indices} \tag{2.25}$$

This leads to an extremely simple form for the d_{ijk} tensor for the zincblende structure:

$$d_{ijk} = \begin{bmatrix} 0 & 0 & 0 & d_{14} & 0 & 0 \\ 0 & 0 & 0 & 0 & d_{14} & 0 \\ 0 & 0 & 0 & 0 & 0 & d_{14} \end{bmatrix} \tag{2.26}$$

There are only three non-zero components of d_{ijk}, all of which are equal! ($d_{14} = d_{123}$ is equal to $d_{25} = d_{213}$ is equal to $d_{36} = d_{312}$.) It is important to note that crystal symmetry leads to this form of the susceptibility tensor *despite* Kleinman symmetry, which holds only for lossless media. The crystal axes are chosen according to the IRE convention [17] which selects the axes of highest symmetry for (x,y,z), in this case the (100) axes. The simplified form of the susceptibility tensor results in equation (2.23) appearing as:

$$\begin{bmatrix} P_x \\ P_y \\ P_z \end{bmatrix} = \varepsilon_o \begin{bmatrix} 0 & 0 & 0 & d_{14} & 0 & 0 \\ 0 & 0 & 0 & 0 & d_{14} & 0 \\ 0 & 0 & 0 & 0 & 0 & d_{14} \end{bmatrix} \begin{bmatrix} E_x^2 \\ E_y^2 \\ E_z^2 \\ 2E_yE_z \\ 2E_xE_z \\ 2E_xE_y \end{bmatrix} e^{i(\vec{k}_1+\vec{k}_2-\vec{k}_3)\cdot\vec{r}} \quad (2.27)$$

2.7 THEORETICAL CALCULATIONS OF $\chi^{(2)}$

There are several successful models used to predict values of nonlinear susceptibility. The first attempt to calculate $\chi^{(2)}$ was done by Miller [18] who related $\chi^{(2)}$ to $\chi^{(1)}$ by the relation,

$$\chi^{(2)}_{ijk}(\omega_1+\omega_2, \omega_1, \omega_2) = \delta_{ijk}(\omega_1, \omega_2)\ \chi^{(1)}_{ii}(\omega_1+\omega_2)\ \chi^{(1)}_{jj}(\omega_1)\ \chi^{(1)}_{kk}(\omega_2) \quad (2.28)$$

where δ is a constant. Although δ, known as Miller's delta, is not a true constant its variation with material is remarkably small compared to $\chi^{(2)}$, varying by less than $\pm 50\%$ for crystals of a given symmetry class [19]. The most striking result from this equation is that $\chi^{(2)}$ can be calculated solely on a knowledge of the linear properties of the material. Furthermore, it states that a material with a high electronic polarizability (i.e. index of refraction) will also have a large optical nonlinearity. However, the symmetry of the medium is not explicitly reflected in this equation.

Yariv [20] outlines a classical anharmonic oscillator model that gives expressions for $\chi^{(2)}$. There are also several quantum mechanical models for calculating susceptibilities, including $\chi^{(2)}$ and $\chi^{(3)}$. Jha and Bloembergen [21] and Flytzanis and Ducuing [22,23] developed a bond model that used ground state electronic wavefunctions to calculate bond polarizability from which the nonlinear susceptibility was determined. These calculations

were performed specifically for tetrahedral compounds. Refinements on these calculations were later performed by Levine [24] and Choy, Ciraci and Byer [25].

Tang and Flytzanis [26] developed a charge transfer model which calculates the dipole induced by an applied electric field. This leads to an expression for polarizability which can be used to calculate $\chi^{(2)}$. The details of these model calculations are complex and provide little physical insight, so they are considered outside the scope of this work. For a more complete review of these calculations see Ref. [27].

CHAPTER 3 - THE SURFACE-EMITTING WAVEGUIDE

This chapter describes the operating principles of the surface-emitting waveguide and derives a formula for calculating the harmonic power conversion efficiency.

3.1 COUNTERPROPAGATING BEAMS

A waveguide is an ideal environment for second harmonic generation because of the high field intensities and extended interaction lengths that can be achieved with a confined beam. In a slab waveguide made from a crystalline material (for example, the $\bar{4}3m$ point group), nonlinear mixing of counter-propagating beams generates a surface-emitted beam at the sum frequency. Optical frequencies corresponding to the communications wavelength range of 1.0-1.55 μm can produce surface emission in the red, green and blue spectral region.

Consider a situation where two arbitrary modes are present, as in Fig. 3.1. The propagation constant of a waveguide is defined as,

$$\beta = n_{eff}\, k_o^{(\omega)} \tag{3.1}$$

where n_{eff} is the effective index of the guided mode and $k_o^{(\omega)}$ is the vacuum propagation constant of the guided light. This three-beam interaction - consisting of two fundamental input beams and one sum-frequency output beam - must obey momentum conservation. For the case where the modal propagation constants are different, say $\beta_1 > \beta_2$, this will lead to emission at an angle, θ, to the surface normal in accordance with momentum conservation given by:

$$\cos\theta = \frac{\Delta\beta}{k_o^{(2\omega)}} \tag{3.2}$$

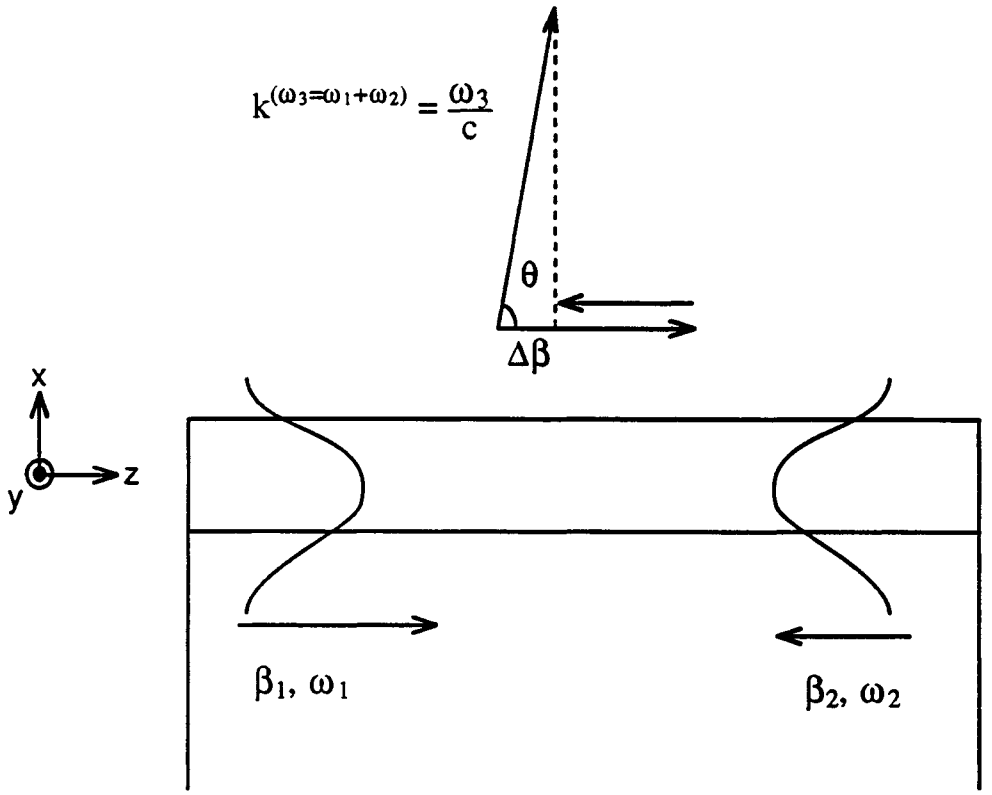

Fig. 3.1: The nonlinear mixing of two counter-propagating beams in a waveguide results in the surface emission of a sum-frequency beam. The angle of surface emission is determined by momentum conservation of the interacting beams, as depicted by the vector addition of the arrows representing the propagation constants. It is clear from the diagram that $\cos\theta = \Delta\beta / k$ where $\Delta\beta = \beta_1 - \beta_2$ and $k_0^{(2\omega)}$ is the vacuum propagation constant of the surface-emitted, sum-frequency beam.

In the specific case of second harmonic generation where the two beams have the same frequency, it is still possible to get non-vertical surface emission due to waveguide birefringence. In this case, the vacuum propagation constant of the fundamental is equal to half that of the harmonic, leading to a simplified form of (3.2) :

$$\cos\theta = \frac{\Delta n_{eff}}{2} \tag{3.3}$$

where Δn_{eff} is the difference between the effective indices of the two interacting modes. Clearly, the angle of surface emission depends directly on the difference in modal effective index.

3.2 CRYSTAL ORIENTATION

The waveguides used in this work were grown on (100) oriented crystal surfaces. The cleavage planes that were opened up to form the optical cavity were (110) planes, meaning the coordinate system defined for the waveguide {x, y, z} does not match the principal axes of the crystal {x',y',z'}, as shown in Fig. 3.2. A TE or TM mode propagating in the z-direction in the guide will have components in terms of the principal axes given by

$$\begin{aligned} \vec{E}_{TE} &= E_{TE}\,\hat{y} = \frac{1}{\sqrt{2}} E_{TE}\,\hat{y}' + \frac{1}{\sqrt{2}} E_{TE}\,\hat{z}' \\ \vec{E}_{TM} &= E_{TM}\,\hat{x} = \quad E_{TM}\,\hat{x}' \end{aligned} \tag{3.4}$$

where we have ignored the small component of $\vec{E}_{TM}$ in the yz-plane. (As well, the phase terms have been omitted for simplicity.) An examination of Equation (2.27) reveals that TE-polarized modes alone will produce a non-linear dipole moment. This means that a pure TE modes in the waveguide will generate a second-harmonic signal. In contrast, a pure TM mode alone produces no dipole moment at all. Despite this, the TE polarization alone cannot lead to surface emission. Notice that the resultant polarization is oriented in the x-direction and a dipole *cannot* radiate in the direction of polarization! This *can* lead to

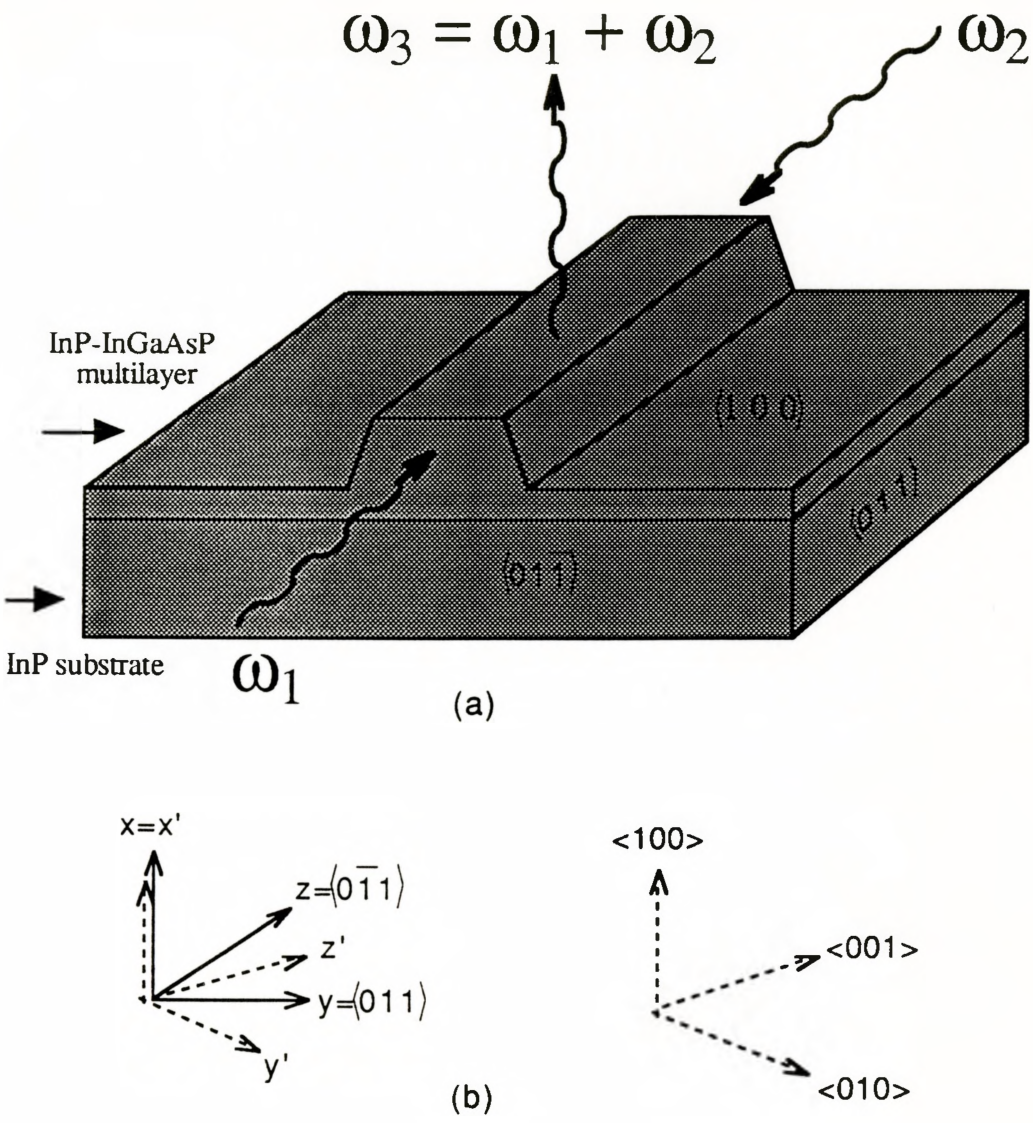

Fig. 3.2: (a) Diagram showing ridged surface-emitting waveguide (SEWG). The light is coupled to the ridge from opposite sides, leading to an emission from the surface at the sum frequency. The crystal planes defining the waveguide facets and surface are shown. These sides are determined by the preferred cleavage planes of the crystal and the substate orientation. (b) Comparison of the principal axes of the crystal to the {x, y, z} coordinate system chosen for the waveguide. The z-axis is the direction of propagation in the waveguide.

SHG in the plane of the waveguide, resulting in emission of a harmonic signal from the end facets of a laser [28] or waveguide cavity.

Equation (2.27) requires that a TE mode and a TM mode be present in the waveguide in order to generate a nonlinear polarization that can produce surface emission. This interaction will generally not yield a beam that is emitted exactly perpendicular to the surface because the two modes will invariably have different propagation constants. However, in some situations it may be preferable to use a pure TE mode in the interaction. This simplifies restrictions on input polarization and allows easier integration with lasers, which typically run TE. A SEWG based on a pure TE interaction is possible [29] if the waveguide is grown on (110) or (111) oriented substrate. However, due to the cleaving properties of (111) and (110) substrates, it was decided to fabricate the device on (100) substrate only.

Substituting (3.4) into (2.29) yields the polarization in terms of the principal crystal axes:

$$\begin{aligned} P_{y'} &= \sqrt{2}\,\varepsilon_o\, d_{14}\, E_{TE}\, E_{TM}\, \hat{y}' \\ P_{z'} &= \sqrt{2}\,\varepsilon_o\, d_{14}\, E_{TE}\, E_{TM}\, \hat{z}' \end{aligned} \tag{3.5}$$

In terms of the original waveguide coordinate system, we find the polarization is totally in the z-direction, as given by:

$$P_z = \sqrt{P_{y'}^2 + P_{z'}^2}\;\hat{z} \;=\; 2\,\varepsilon_o\, d_{14}\, E_{TE}\, E_{TM}\, \hat{z} \tag{3.6}$$

or, including phase relations from (2.29),

$$P_z \exp[\, ik_3 z] = 2\,\varepsilon_o\, d_{14}\, E_{TE}\, E_{TM} \exp[\, i\Delta\beta z]\, \hat{z} \tag{3.7}$$

Note that (3.7) is the exact relation given by (2.27) even though we have performed a change of coordinate systems.

3.3 ELECTRIC FIELD AT THE FUNDAMENTAL FREQUENCY

According to Equation (2.27), the strength of the dipole moment at any point is proportional to the product of the TE and TM fields. These fundamental fields are optical waveguide modes with known, calculable mode shapes [30]. The small pump-depletion approximation was used, which assumes a low-efficiency second harmonic generation process, so the mode intensity remains constant along the waveguide length. If we ignore the variation in the field intensity in the y-direction then the electric field strength is only a function of x. The spatially varying term in the electric field will be denoted as $E_{TE}(x)$ and $E_{TM}(x)$ with a + or - to denote forward or backward travelling wave.

Throughout this work, only the 0^{th} order waveguide modes are considered when performing calculations. The multilayer waveguide was treated as a simple 3-layer slab waveguide in all calculations even though it is straightforward (but lengthy!) to perform the calculation for an n-layer waveguide with existing algorithms. This was done to improve calculation speed and simplicity and to enable comparison with the work of Normandin [4,5].

The guided light is governed by Maxwell's Equations and the dielectric boundary conditions. In each layer the light obeys the equation,

$$\nabla^2\vec{E}(\vec{r}) + k_o^2\, n^2(\vec{r})\,\vec{E}(\vec{r}) = 0 \tag{3.8}$$

where k_o is the vacuum propagation constant and $n(\vec{r})$ is the material refractive index as a function of position. The solution for a TE mode is given by:

$$\vec{E}(\vec{r},t) = E_{TE}(x)\exp[i(\beta z-\omega t)]\,\hat{y} \tag{3.9}$$

where β is the parallel component of the wavevector satisfying continuity requirements across the boundaries (i.e. the guided mode propagation constant). Solutions for $E_{TE}(x)$ in the three sections of the waveguide - substrate, guiding slab layer, and superstrate (air) - are given by,

$$
\begin{aligned}
E_{TE}(x) &= E_o\, e^{-qx} && x>0 \\
E_{TE}(x) &= E_o\left(\cos(k_p x) - \frac{q}{k_p}\sin(k_p x)\right) && -h<x<0 \\
E_{TE}(x) &= E_o\left(\cos(k_p h) + \frac{q}{k_p}\sin(k_p h)\right) e^{p(x+h)} && x<-h
\end{aligned}
\qquad (3.10)
$$

where k_p is the normal component of wavevector (subject to continuity at the boundaries), p and q are real numbers and h is the thickness of the guiding layer. These constants are subject to the conditions,

$$
\begin{aligned}
k_p &= \left(n_2^2 k_o^2 - \beta^2\right)^{1/2} \\
q &= \left(\beta^2 - n_1^2 k_o^2\right)^{1/2} \\
p &= \left(\beta^2 - n_3^2 k_o^2\right)^{1/2}
\end{aligned}
\qquad (3.11)
$$

where n_1, n_2, and n_3 are the refractive indices in the superstrate, guide layer and substrate respectively. The boundary conditions produce the following dispersion relation which can be solved to find the correct values of q, p, k_p, and β:

$$
\tan(k_p h) = \frac{p+q}{k_p\left(1 - \frac{pq}{k_p}\right)} \qquad (3.12)
$$

The solution is found numerically by varying β until (3.12) is satisfied. The effective index of the waveguide is defined as:

$$
n_{eff} = \frac{\beta}{k_o} \qquad (3.13)
$$

These results are summarized in Figure 3.3 .

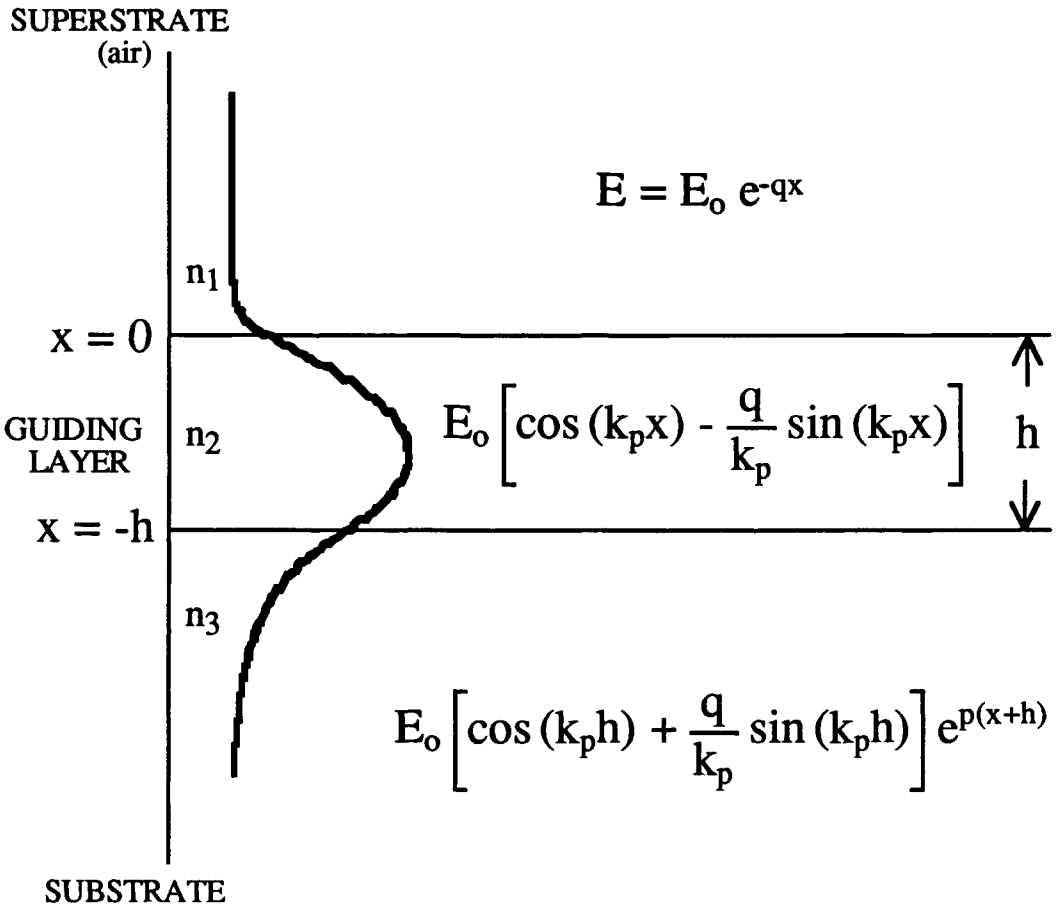

Fig. 3.3: Mode shape for a three layer slab waveguide. The guiding layer has a thickness, h, while the super- and sub-strates are considered infinitely thick. The solution for the TE mode electric field amplitude is shown. The guide-air interface is defined as x=0 and positions inside the waveguide are negative. The refractive indices of the superstrate, guiding layer and substrate are n_1, n_2, and n_3 respectively.

3.4 NEAR-FIELD SURFACE EMISSION PATTERN

Experimentally, a single, coherent source was coupled into the waveguide and the counter-propagating beam was supplied by the back-reflection from the far facet. The pulsed Nd:YAG laser used in the experiments provided an unpolarized source. Thus, the power coupled into the TE and TM modes of the waveguide were approximately equal. When using a semiconductor laser in CW mode, the input polarization had to be oriented at ~45° to the waveguide to ensure good coupling to both modes.

In a single-mode guide, there are now two modes propagating in each direction, TE^+, TE^-, TM^+, TM^-. The two TE modes form a standing wave in the optical cavity (as does the TM) with a profile that appears as:

$$E_{TE} = E_{TE}^{+}(x)\ e^{i(\omega t-\beta_{TE}z)} + E_{TE}^{-}(x)\ e^{i(\omega t+\beta_{TE}z)}$$

$$= 2\,E_{TE}(x)\cos(\beta_{TE}z)\,e^{i\omega t} \qquad (3.14)$$

and

$$E_{TM} = 2\,E_{TM}(x)\cos(\beta_{TM}z)\,e^{i\omega t}$$

where we have assumed the counter-propagating modes have the same field strength. (This is a poor approximation unless the far facet has a highly reflective coating but the subsequent result is not far-reaching in terms of the scope of this work.) As the TE and TM light mix nonlinearly, they beat against each other, resulting in a spatial modulation of the nonlinear polarization across the length of the guide. By substituting (3.14) into (2.29) the modulation takes the form:

$$P_{NL}\hat{z} = 2\varepsilon_o d_{14}\,E_{TE}\,E_{TM}\,\hat{z} \qquad (3.15)$$

$$= 8\,\varepsilon_o d_{14}\,E_{TE}(x)\,E_{TM}(x)\left[\cos(\Delta\beta\,z) + \cos((\beta_{TE}+\beta_{TM})\,z)\right]\,e^{i2\omega t}\,\hat{z}$$

The first cosine term is the beating term and is readily observable in Figure 3.4 by imaging the near-field emission pattern. The second cosine term is a rapidly varying term and is too

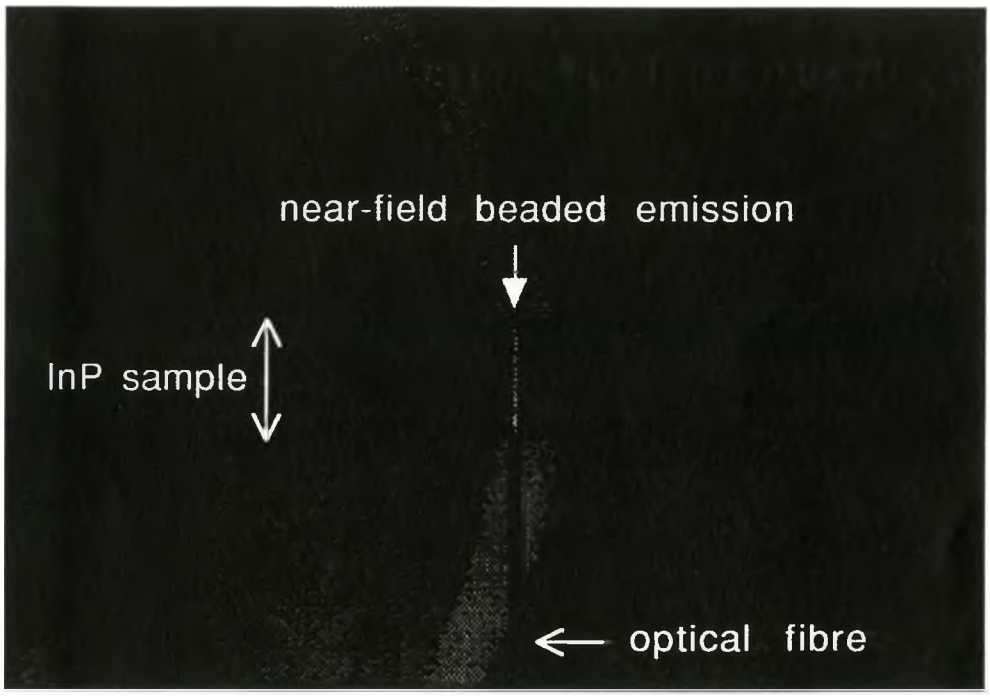

Fig. 3.4: Near-field surface emission pattern of second-harmonic signal. Note the beaded appearance of the harmonic light due to the beating of the TE and TM optical modes (this is not caused by lack of resolution in the image). Light at 1.32 μm wavelength is coupled to the waveguide via an optical fibre. The counter-propagating beam is supplied by the back-reflection from the far facet. The picture was taken with a thermoelectrically cooled CCD camera.

fast to be observed. The beat spacing represents the second method of measuring the difference in propagation constants between two modes by using surface emission. Note that the beating does not occur if the two interacting beams are at different frequencies. This is because the two counter-propagating waves would not maintain a constant phase relationship or, mathematically, the time-dependent phase term would not be factorable in (3.14). In this case, the output would appear uniform across the guide.

3.5 RADIATION FROM HARMONIC POLARIZATION

So far we have discussed a nonlinear interaction of electric fields that leads to the generation of a polarization field at the sum (harmonic) frequency. This section will describe how the polarization field radiates to produce a surface-emitted beam. We will only consider the specific case of SHG, and shall denote the fundamental frequency as ω.

3.5.1 Maxwell's Equations

The nonlinear polarization must now be considered as a radiating dipole field. This appears as a driving term in Maxwell's equations, which produces an electromagnetic field:

$$\nabla^2 \vec{E}(2\omega) - \mu_o \varepsilon \frac{\partial^2 \vec{E}(2\omega)}{\partial t^2} = \mu_o \frac{\partial^2 \vec{P}_{NL}(2\omega)}{\partial t^2} \tag{3.16}$$

The polarization will have the form:

$$\vec{P}_{NL} = \hat{z}\, P_{NL}(x)\, e^{i(\Delta\beta\, z - 2\omega t)} \tag{3.17}$$

so we attempt a trial solution for E of a similar form:

$$\vec{E} = \hat{z}\, E(x)\, e^{i(\Delta\beta\, z - 2\omega t)} \tag{3.18}$$

Substituting (3.17) and (3.18) into (3.16) yields the equation,

$$\left(\frac{\partial^2}{\partial x^2} + k_x^2\right) \vec{E}(x) = -\frac{k^2}{\varepsilon}\, P_{NL}(x)\, \hat{z} \tag{3.19}$$

where

$$k_x^2 = k^2 - \Delta\beta^2 \tag{3.20}$$

and

$$k = \frac{(2\omega)\, n}{c} = k_o\, n \tag{3.21}$$

where k is the bulk propagation constant of the second harmonic wave in the material, n is the refractive index at frequency 2ω and c is the speed of light.

3.5.2 Green's Function Formalism

The solution of this equation is obtained by using the Green's function formalism. The polarization is replaced by a delta function plane source located at x' to obtain,

$$\left(\frac{\partial^2}{\partial x^2} + k_x^2\right) \vec{E}_g(x) = -\frac{k^2}{\varepsilon}\, \hat{z}\, \delta(x, x') \tag{3.22}$$

where $E_g(x)$ is the Green's function electric field. The solution to (3.22) is,

$$\vec{E}_g(x) = -\frac{ik}{2\varepsilon}\, \hat{z} \exp\left(-ik_x |x - x'|\right) \tag{3.23}$$

where x is the observation point i.e. this expression gives the value of $E_g(x)$ at a distance $|x - x'|$ from the source plane. Substituting this into (3.18), the full expression is obtained:

$$\vec{E}_g(x) = -\frac{ik}{2\varepsilon}\, \hat{z} \exp\left[i(-k_x|x-x'| - \Delta\beta z + 2\omega t)\right] \tag{3.24}$$

This is the expression for radiation from a plane sheet source in the y-z plane. It consists of 2 half-plane waves as shown in Fig. 3.5, one radiated towards the surface and the other into the substrate making an angle theta with the y-z plane given by

$$\cos\theta = \frac{\Delta\beta}{k} \tag{3.25}$$

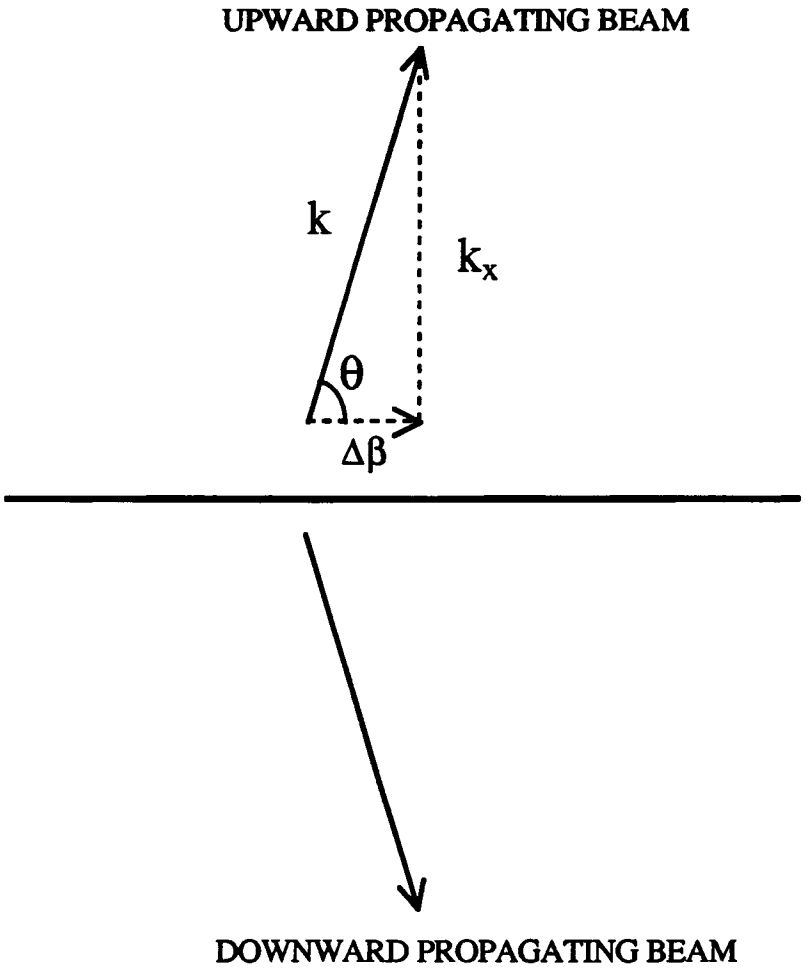

Fig. 3.5: Upward and downward waves generated from a radiating dipole sheet. The downward propagating wave is lost to the substrate and can be ignored in a first-order approximation.

Note that (3.25) gives the direction of propagation *inside* the waveguide, while the earlier equation (3.2) is strictly the angle of emission from the guide after refracting through the semiconductor-air interface.

3.5.3 Electric Field at the Waveguide Surface

We are interested in calculating the total electric field at the surface (x=0), so we consider only the upward-propagating wave. We neglect any interface reflections, including any reflections of the downward propagating wave. The total contribution from all of the radiating sheets is found by integrating (3.24) and including the polarization strength,

$$\vec{E}(x,z) = \int \frac{-ik}{2\varepsilon} \hat{z}\, P_{NL}(x')\exp[-ik_x(x-x')]\, dx' \cdot \exp[-i\Delta\beta z] \qquad (3.26)$$

evaluating at x=0. The limits of integration are the extent of the nonlinear material. The superstrate is typically air, which is a linear medium ($P_{NL}= 0$), so the limits are $-\infty \rightarrow 0$. For small emission angles (typical of modes with similar propagation constants, as with TE and TM 0th order modes), we can make the approximation,

$$k_x = \sqrt{k^2 - \Delta\beta^2} \approx k \qquad (3.27)$$

Combining (3.27) and (3.21) with (3.26), the net electric field at the surface is given by,

$$\vec{E}(x,z) = \int_{-\infty}^{0} \frac{-ik}{2\varepsilon} \hat{z}\, P_{NL}(x') \exp[ik_o n(x')\cdot x']\, dx' \cdot \exp[-i\Delta\beta z] \qquad (3.28)$$

3.6 CORRECTIONS AND APPROXIMATIONS

This is the solution first presented by Normandin and Stegeman [5] and later by Vakhshoori and Wang [8]. Equation (3.28) is accurate for bulk waveguide material but ignores boundary reflections, changes in refractive index, and the effects of the downward propagating wave - in other words, a failure to treat the waveguide as an optically active multilayer stack. The exact solution to this problem was recently published by Vakhshoori [29] using a matrix formalism.

These straightforward but lengthy calculations presented in [29] aren't necessary to get an accurate estimate of the SH output. This is because the boundary reflections are small. For example, a very large index step of $\Delta n=0.5$ leads to only a ~5% reflection coefficient for the electric field. Furthermore, the designed and grown structures were very close to $\lambda/2$ multilayer stacks (at the harmonic wavelength) meaning they were optically transmitting. For these reasons, the reflections can be ignored, as well as the effects of the downward propagating wave. However, we are confined to use structures that are on or near a $\lambda/2$ stack for the modelling to be accurate. These structures will be fairly broadband due to the small reflection coeffecients, allowing a fair amount of variation in layer thickness before our model breaks down.

Although reflections can be ignored in Eq.(3.28), it is not appropriate to ignore variations in refractive index. Specifically, this refers to the exponential phase term $\exp[ik_o n(x')x]$, which represents the optical phase change as a wave travels from the point of origin (the dipole sheet at $x'<0$) to the surface,

$$\phi = k_o n(x')\, x' = \frac{2\pi n^{(2\omega)}}{\lambda_o^{(2\omega)}}\, x' \qquad (3.29)$$

where n and λ are evaluated for the harmonic frequency. If the refractive index varies with depth, as in a multilayer then the total phase change over the distance $|x'|$ is better expressed as,

$$\phi = -\frac{2\pi}{\lambda_o^{(2\omega)}} \int_{x'}^{0} n^{(2\omega)}(x)\, dx \tag{3.30}$$

Even though the index variations between layers may be very small (say $\Delta n = 0.3$ or 10%) the net difference in optical path length may be significant. Over 10 periods of the structure - or about 5 optical wavelengths - the difference will be ~50% of one optical cycle. This represents a phase difference of 180° compared with the uncorrected case; the contribution from a dipole sheet that is 5 optical wavelengths from the surface will have the wrong sign! The inclusion of this phase correction represents a significant improvement in the model's accuracy over previous work. The proper, phase corrected expression for electric field is,

$$\vec{E}(x,z) = \int_{-\infty}^{0} \frac{-ik}{2\varepsilon} \hat{z}\, P_{NL}(x') \exp\left[-ik_o \int_{x'}^{0} n^{(2\omega)}(x)\, dx\right] dx' \cdot \exp[-i\Delta\beta z] \tag{3.31}$$

3.7 CALCULATION OF SECOND HARMONIC POWER

Before proceeding, several identities will be introduced that will be useful in simplifying our equations:

$$\varepsilon = \varepsilon_o(1 + \chi^{(1)}) = \varepsilon_o n^2$$

$$Z = \sqrt{\frac{\mu_o}{\varepsilon_o}} \tag{3.32}$$

$$c = \frac{1}{\sqrt{\mu_o \varepsilon_o}}$$

where Z is the impedence of free space. By combining (3.32) with (3.21) yields,

$$\frac{k}{\varepsilon} = \frac{2\omega Z}{n^{(2\omega)}} \tag{3.33}$$

which is then substituted into (3.31).

Although the reflections throughout the multilayer have been ignored, we must include the Fresnel transmission [31] at the semiconductor-air interface, given by,

$$t = \frac{2\, n^{(2\omega)}}{n^{(2\omega)} + 1} \tag{3.34}$$

where $n^{(2\omega)}$ is the index of refraction of the semiconductor at the surface. Combining (3.33) and (3.34) with (3.31) yields,

$$\vec{E}(x,z) = -i2\omega Z\, \hat{z}\, \frac{n^{(2\omega)}}{n^{(2\omega)} + 1}\, \exp[-i\Delta\beta z] \cdot S \tag{3.35}$$

where the definition of the S-integral has been introduced as,

$$S = \int_{-\infty}^{0} \frac{P_{NL}(x')}{n^{(2\omega)}(x')} \exp\left[-ik_o \int_{x'}^{0} n^{(2\omega)}(x)\, dx\right] dx' \tag{3.36}$$

The harmonic power is given by the Poynting vector which yields a time-averaged value given by,

$$\left\langle \vec{S}_{av} \right\rangle = \frac{1}{2}\, \mathrm{Re} \left\langle \vec{E}_{top} \times \vec{H}^{*}_{top} \right\rangle \qquad \left[\frac{W}{m^2}\right] \tag{3.37}$$

For plane waves in vacuum, the E and H fields are related by,

$$\left|\vec{H}\right| = \frac{1}{c\mu_o} \left|\vec{E}\right| = \frac{1}{Z} \left|\vec{E}\right| \tag{3.38}$$

Combining (3.37) and (3.38) with (3.35) the expression for the harmonic power is,

$$\left\langle \vec{S}_{av} \right\rangle = 4\omega^2 Z \left(\frac{n^{(2\omega)}}{n^{(2\omega)} + 1}\right)^2 S \cdot S^{*}\, \hat{k} \tag{3.39}$$

where $\hat{k}$ is the unit direction vector making an angle θ with the surface. (Note that the exponential term in (3.35) is not present in (3.39); this term determines the angle of emission, as per (3.24) .)

The full expression for the S-integral is achieved by substituting the nonlinear polarization (3.6) into (3.36) to yield,

$$S = \int_{-\infty}^{0} 2\varepsilon_0 d_{14} \frac{E^{+}_{TE}(x')E^{-}_{TM}(x')}{n^{(2\omega)}(x')} \exp\left[-ik_0 \int_{x'}^{0} n^{(2\omega)}(x)\, dx\right] dx' \qquad (3.40)$$

where the expressions for the electric field are given by the mode profiles in (3.10). Equation (3.39) represents the second harmonic power per square meter of radiating waveguide surface and depends on the powers of the two counter-propagating modes through the S-integral. The total power radiated from the surface is then,

$$P_{SH} = \langle S_{av} \rangle \cdot A = \langle S_{av} \rangle \cdot l\ w \qquad [W] \qquad (3.41)$$

where A is the total radiating area, l is the length in the direction of waveguide propagation and w is the width. For consistency with previous work, the dimensions of the guide are assumed to be (l w) = 10mm x 1mm.

3.8 NONLINEAR CROSS-SECTION

It is appropriate to introduce a nonlinear cross-section to describe the interaction efficiency as,

$$A_{NL} \equiv \frac{P_{SH}}{P^{+}\, P^{-}} \qquad \left[\frac{1}{W}\right] \qquad (3.42)$$

where $P^{+,-}$ are the powers in the two fundamental guided modes. A_{NL} is a constant for a given waveguide, irregardless of input power. This is inherent to nonlinear processes. If the total input power in the two modes is doubled, the second harmonic power increases by

a factor of 4x. Clearly, any efficiency can be obtained with sufficiently large powers until either the small pump depletion approximation breaks down or the practical power limit for waveguide coupling is reached (i.e. burning the waveguide facet with the incident light). It is this nonlinear cross-section that must be maximized to produce efficient second harmonic generation.

The power in the fundamental mode is given by the integral of the Poynting vector over the cross-sectional area of the guide, which appears for the TE mode as,

$$\left\langle \vec{P}^{+} \right\rangle = \int \left\langle \vec{E}_{TE}(x) \times \vec{H}^{*}_{TE}(x) \right\rangle dA$$

$$= w \cdot \int_{-\infty}^{\infty} \left\langle \vec{E}_{TE}(x) \times \vec{H}^{*}_{TE}(x) \right\rangle dx \qquad (3.43)$$

where the field strength is considered a constant in the y-direction over some finite width, w, so that E and H are only functions of x. The time-averaged cross product yields,

$$\left\langle \vec{E} \times \vec{H}^{*} \right\rangle = \frac{n_{eff}}{Z} |E|^2 \, \hat{z} \qquad (3.44)$$

Re-writing (3.43) with (3.44) we find,

$$\left\langle \vec{P}_{TE} \right\rangle = \frac{w \, n_{eff}}{Z} \int_{-\infty}^{\infty} |E|^2 \, dx \quad \hat{z} \qquad (3.45)$$

The electric field can be written as,

$$E(x) = C \, \xi(x) \qquad (3.46)$$

where C is the magnitude of the electric field. The electric field in the fundamental mode is normalized per unit width of the guide using,

$$\int_{-\infty}^{\infty} \xi^2(x)\, dx = 1 \tag{3.47}$$

Combining (3.45) - (3.47), the fundamental mode power is given by ,

$$P^+ = \frac{w\, n_{eff}}{Z} C^2 \quad [W] \tag{3.48}$$

By substituting the expression for the electric field (3.46) into the S-integral (3.40), the expression for total SH power becomes,

$$P_{SH} = 4\omega^2 Z\, (l\, w) \left(\frac{n^{(2\omega)}}{n^{(2\omega)} + 1}\right)^2 C^4\, S{\cdot}S^* \quad [W] \tag{3.49}$$

By solving (3.48) for C^2 and substituting into (3.49), an expression for the harmonic power is obtained in terms of the fundamental mode powers,

$$P_{SH} = 4\omega^2 Z^3 \left(\frac{l}{w}\right) \left(\frac{n^{(2\omega)}}{n^{(2\omega)} + 1}\right)^2 S{\cdot}S^*\; P^+ P^- \quad [W] \tag{3.50}$$

From our definition in (3.42), the expression for A_{NL} is clearly given by,

$$A_{NL} = \frac{4\omega^2 Z^3}{n_{eff}^2} \frac{l}{w} \left(\frac{n^{(2\omega)}}{n^{(2\omega)} + 1}\right)^2 S{\cdot}S^* \quad \left[\frac{1}{W}\right] \tag{3.51}$$

This completes the theoretical derivation of the nonlinear cross-section of the SEWG.

CHAPTER 4 - ALGORITHM FOR DESIGN AND OPTIMIZATION OF THE SEWG

This chapter describes the basis for designing the SEWG and the QuickBASIC algorithm implemented to calculate the nonlinear cross-section. The theoretical predictions from this algorithm are also presented.

4.1 OPTIMIZATION OF A_{NL}

Equation (3.51) is the central equation governing the performance of the surface emitting waveguide. The main goal of this work is to design an InP-based waveguide with the maximum value of A_{NL} achievable. An examination of this equation quickly reveals that this problem reduces to maximizing the S-integral (3.40).

In order to best understand how to perform the optimization, the physical significance of all terms in the S-integral must be kept in mind. The $P_{NL}(x)$ term represents the radiating source strength of the "polarization sheet" at a depth x below the surface; n(x) is the (complex) refractive index at depth x; and the exponential term represents the optical phase change as the EM field emitted from the source travels the distance |x| to the surface. The most obvious parameter to maximize is d_{14}, which supports the move to the III-V material system. There is also evidence to suggest choosing InP over GaAs because of possibly larger d_{14} [23-25].

However, much of the second harmonic light destructively interferes to produce very low efficiency output. If we consider two dipoles of equal strength radiating in phase that are $\lambda/2$ apart, the sum of their output will cancel in the far-field. This very nearly describes what happens inside a slab waveguide, except for a variation of dipole strength with position. The dipole strength is proportional to the product of the fundamental frequency electric field strengths at a given depth in the waveguide (as in Eq. 3.40). A

vertical slice through the waveguide represents a plane of constant phase for the fundamental waveguide modes. Hence, all of the second-harmonic dipoles generated along this plane by the nonlinear mixing of the fundamental fields are radiating in phase with each other. For any dipole sheet inside the waveguide, another sheet that is a distance of $\lambda/2$ away will tend to cancel it out. The end result is very low nonlinear cross-section, as reported in early SEWG experiments. The problem outlined here is one of phase matching to reduce destructive interference, as described in Chapter 1. However, the second harmonic beam propagates perpendicular to the fundamental instead of parallel to it, as found in standard SHG schemes.

4.1.1 Constructive Interference of Harmonic Plane Waves

To avoid cancellation of the two dipoles, one of them may be removed by growing a linear material on top of a nonlinear material. The best configuration would be a $\lambda/2$ stack where the layers alternate as linear-nonlinear-linear-nonlinear. The linear layers act as phase shifting regions, so that the light-producing nonlinear regions will add constructively. However, it is not possible to reliably grow a linear material on top of the nonlinear III-V crystal, since the two materials will necessarily have different crystal structures.

At present, we are limited to growing two (or more) nonlinear materials together. In this case, a difference in d_{14} between two different materials can be utilized to produce non-zero cancellation between paired dipole sheets. An examination of the S–integral, Eq. (3.40), reveals that the second-harmonic dipole strength is inversely proportional to the refractive index. Hence, a vertical index step in the waveguide will also result in incomplete cancellation of dipoles that are $\lambda/2$ thickness apart. Therefore, the nonlinear cross-section of the SEWG may be increased by maximizing the difference in nonlinear coefficient and/or refractive index between layers in the multilayer stack.

The phase term of the S-integral is also strongly dependent on refractive index (refer to Section 3.6, particularly Eq.(3.30)). In general, a multilayer stack with arbitrary choice of layer thickness and material composition (which determines nonlinear coefficient and refractive index) can result in increased *destructive* interference due to this phase term, yielding an even lower nonlinear cross-section than would be obtained with a simple slab

waveguide! Hence, the choice of layer thickness is critical in tailoring the phase term of the harmonic plane wave. Given a particular pair of materials, the layer thicknesses should be chosen to optimize the constructive interference and, hence, maximize the nonlinear cross-section.

To demonstrate the basis for the optimization mathematically, the nonlinear cross-section from a two-layer stack will be calculated using Eqs. (3.40) and (3.51). To simplify the integration, the electric field will be considered constant, so it can be factored out. All constants will be lumped together into one global constant, K. First, consider the contribution, S_1, to the S-integral (3.40) from a single homogeneous layer at the surface of the waveguide with thickness, d_1, and refractive index, n_1. The contribution S_1 is:

$$S_1 = K \int_{-d_1}^{0} \frac{\chi_1^{(2)}}{n_1} e^{[-ik_o n_1 \cdot x]} \, dx' \tag{4.1}$$

$$= \frac{K \chi_1^{(2)}}{ik_o n_1^2} \left(1 - e^{[ik_o n_1 d_1]}\right)$$

Clearly, when the phase term satisfies $k_o n_1 d_1 = 2\pi q$ (q=integer), the layer contributes nothing to the second-harmonic output. Solving for the layer thickness, $d_1 = q\lambda_1$, so for the worst case the layer thickness is equal to an integral number of optical wavelengths. Similarly, the contribution of a second layer of thickness d_2 and refractive index n_2 that lies below the first layer is:

$$S_2 = \frac{K \chi_2^{(2)}}{ik_o n_2^2} \left(1 - e^{[ik_o n_2 d_2]}\right) e^{[-ik_o n_1 d_1]} \tag{4.2}$$

where the only difference between S_2 and S_1 is the second exponential phase term which represents the extra phase shift from the light in layer 2 traveling through layer 1 to the surface. Upon summing the contributions from the layers together, one gets,

$$S = \frac{K}{ik_o}\left[\frac{\chi_1^{(2)}}{n_1^2}\left(1 - e^{[ik_o n_1 d_1]}\right) + \frac{\chi_2^{(2)}}{n_2^2}\left(1 - e^{[ik_o n_2 d_2]}\right) e^{[-ik_o n_1 d_1]}\right] \qquad (4.3)$$

Substitution of Eq.(4.3) into Eq. (3.51) followed by differentiation with respect to d_j (j=1,2) yields the result that S is maximized when $d_j=(q+1/2)\lambda_j$ i.e. the optimum layer thickness is half an optical wavelength (for q=0). Substituting this solution into Eq.(4.3) yields,

$$S = \frac{2K}{ik_o}\left[\frac{\chi_1^{(2)}}{n_1^2} - \frac{\chi_2^{(2)}}{n_2^2}\right] \qquad (4.4)$$

Hence, in this example the nonlinear cross-section depends on the quantity $\chi^{(2)}/n^2$ for each layer and can be optimized by maximizing the difference in this quantity between layers. This analysis included the effects of only two layers but can easily be extrapolated to many layers with similar results. However, this is not conclusive because of the assumption that the electric field is constant throughout the waveguide. A similar analysis that includes the variation of electric field would be difficult and is considered beyond the scope of this work. This result does provide a strong argument for using a half-wave stack and provides an excellent starting point for modeling.

4.1.2 Future Materials

A superior scheme for improving the nonlinear cross-section of the SEWG is to reverse the direction of the second dipole. This would be equivalent to changing the sign in $\chi^{(2)}$ [32]. In this case, the two dipoles add to produce the highest output of any scheme. To achieve this in a III-V material such as InP, the positions of the In and P atoms must be reversed [8]. As mentioned earlier, the second order nonlinear coefficient possesses the same symmetry properties of the lattice, so an inversion of the crystal (i.e. switching the positions of In and P) also causes a change of sign of $\chi^{(2)}$. This technique is called domain inversion or periodic poling. It is very difficult to grow a "domain inverted" region but a method to achieve this has been suggested in [8]. Here, a thin layer of Si consisting of an even number of atomic layers is grown on an InP layer. If a new layer of InP is

grown on top of the Si, it will appear inverted with respect to the underlying layer. Such a growth requires a very expensive MBE technology with excellent control.

4.2 SEWG DESIGN

In this project, we are limited to using "standard" planar molecular beam epitaxy (MBE) and metallorganic chemical vapour deposition (MOCVD) growth techniques, so we are unable to apply any domain inversion scheme to boost the nonlinear cross-section of the SEWG. The only design parameters of the SEWG's multilayer stack that can be varied are composition and thickness of each layer, and the total number of layers for a chosen operating wavelength. These parameters determine index of refraction, nonlinear coefficient and the waveguide properties. A knowledge of these material parameters is all that is necessary for designing the SEWG.

An optimization of the SEWG based on maximizing the nonlinear cross-section was desired. This required creating an algorithm to systematically check all possible layer structures and select the optimum one. Both of these methods require a more rigorous model where no approximations have been made. Such a calculation is very time-intensive and was considered beyond the scope of this work. Instead, a partial optimization was performed, based on an intuitive understanding of the device operation. The theory presented in Section 4.1 suggests that the optimum structure is a $\lambda/2$ multilayer stack. The optimization of the SEWG involved calculating the nonlinear cross-section, as given by Eq. (3.42), for this type of structure. This is presented in Sections 4.3-4.4.

The nonlinear cross-section of the SEWG is low compared to some of the collinear schemes employed in systems using $LiNbO_3$, which can be as high as 40% or more [33]. Typical values of the nonlinear cross-section are in the 10^{-9} range. Hence, when performing an optimization on the SEWG design, incremental improvements in nonlinear cross-section are not significant. Even a factor of 2x improvement in nonlinear cross-section is not considered large at this stage. More important are the trends in performance, which may provide insight into device behaviour. Keeping this in mind, a precise value of material nonlinear coefficient, d_{14}, is not essential because nonlinear cross-section scales with d_{14}, so any error in its value will simply appear in the final measured value of the nonlinear cross-section.

4.2.1 Dispersion of Nonlinear Coefficient

There is little information on the dispersion of nonlinear coefficient with material composition. There are few experimental values for GaAs available and these typically have large experimental errors associated with them. On the other hand, there is virtually no such information available for InP. However, there are numerous values based on theoretical calculations from different models for both GaAs and InP, some of which are tabulated in Table 4.1. It becomes apparent from Table 4.1 that the predicted values of d_{14} vary significantly from model to model. Furthermore, there is no obvious conclusion that InP has a higher nonlinear susceptibility than GaAs. There is also no information available on the InGaAsP quaternary alloys.

Since no experimental values were available, the d_{14} was assumed to be independent of material for calculation purposes. However, if there is an appreciable variation in d_{14} with material, then the measured nonlinear cross-section will be higher than predicted due to incomplete cancellation of paired dipoles (as discussed in Section 4.1). The value of d_{14} for InP-InGaAsP used in the modeling was chosen to be the same as that used for GaAs in the works of Normandin [4,5]. This value is:

$$d_{14} = 1.35 \cdot 10^{-10} \text{ m/V}$$
$$\chi^{(2)} = 2.7 \cdot 10^{-10} \text{ m/V} \qquad (4.5)$$

Despite the lack of information on material nonlinear coefficients, it is still possible to optimize the SEWG using refractive index information, as discussed in Section 4.1.1 (see also Table 4.2).

4.2.2 Material Absorption

The InP-InGaAsP lattice-matched material system has a smaller bandgap relative to the GaAs-AlGaAs system. The bandgap varies from 1.35 eV for InP to 0.75 eV for $In_{0.53}Ga_{0.47}As$, which is the lattice-matched composition with the highest concentration of

TABLE 4.1: Calculated Values of Second Order Optical Coefficient for GaAs and InP Calculated by Various Models †

d_{14} (10^{-12} m/V)

GaAs	InP
-181	
398	587
398	356
256	222
239	
169	142
209.5	
178	
226	136
128	
79.6	

The value of d_{14} is expressed differently here than in Table 1.1. This is a matter of convention, which varies depending on the author. For example, it is common to find the expression for nonlinear polarization written as $P = \chi^{(2)} E_1 E_2$ (used in Table 1.1) instead of the expression used in this work, $P = \varepsilon_0 \chi^{(2)} E_1 E_2$.

Arsenic. In this work, it is simpler to refer to any lattice-matched composition of InGaAsP by its bandgap wavelength. Following the convention used at BNR, a lattice-matched material will be labeled by a Q (for "quaternary") followed by its bandgap wavelength in microns. For example, $In_{0.53}Ga_{0.47}As$ would be denoted as Q1.65 material. The equivalent bandgap wavelength can be calculated using the following formula,

$$\lambda_g = 1.24 / E_g \tag{4.6}$$

where E_g and λ_g are expressed in eV and μm respectively. The compositions of InGaAsP selected to comprise the SEWG must be transparent at 1.3 μm to form a lossless waveguide. Using Eq. (4.6), the minimum bandgap energy of the InGaAsP material must be 0.954 eV to be transparent at 1.3 μm.

The second-harmonic wavelength of a 1.3 μm signal is 650 nm, which has an energy of 1.9 eV. Even InP is strongly absorbing at this wavelength. Therefore, our model must take care of absorption in the calculations. To include this mathematically, the index of refraction at the harmonic wavelength is considered complex:

$$n = n_{Re} + i\, n_{Im} \tag{4.7}$$

where n_{Re} and n_{Im} represent the real and imaginary part of refractive index respectively. This form for the index of refraction can be substituted into the S-integral equation without any loss of generality. A positive imaginary refractive index will act as an attenuating term with the sign convention chosen here.

4.2.3 Choice of $In_{1-x}Ga_xAs_yP_{1-y}$ Material

When choosing material composition in the InP system, there is a trade-off between minimizing material absorption and maximizing the refractive index step between layers. All of the lattice-matched InGaAsP compositions have smaller bandgap than InP, making InP the least absorbing material in the system. Thus, in order to create an index step at every layer and to minimize absorption effects, alternating layers of InP and lattice-matched InGaAsP with composition between InP and Q1.3 is required. This has a tendency to

TABLE 4.2: Index of Refraction Data for Various Compositions of $In_{1-x}Ga_xAs_yP_{1-y}$ Lattice Matched to InP

Material (y = As mole fraction)	InP y= 0.0	Lattice Matched $In_{1-x}Ga_xAs_yP_{1-y}$ y= 0.421	y= 0.495	y= 0.550
Bandgap Energy (eV)	1.35	1.078	1.033	0.992
Bandgap Wavelength (μm)	0.919	1.15	1.20	1.25
Real RI @ 1.3 μm	3.21 *	3.38 *	3.42 *	3.48 *
Real RI @ 650 nm	3.53 †,3.517 #	3.67 ††	3.70 ††	3.72 †
Complex RI @ 650 nm	-0.285 †,-0.293 #	-0.285 †	-0.31 †	-0.362 †
λ/2 thickness (nm)	92.1	88.6	87.8	87.4

* B. Broberg, S. Lindgren, "Refractive Index of $In_{1-x}Ga_xAs_yP_{1-y}$ layers and InP in the transparent wavelength region", *J. Appl. Phys.* **55** (9), 1984, p. 3376.

† H. Burkhard, H.W. Dinges, E. Kuphal, "Optical Properties of $In_{1-x}Ga_xP_{1-y}As_y$, InP, GaAs, and GaP determined by ellipsometry", *J. Appl. Phys.* **53** (1), 1982, p. 655.

O.J.Glembocki, H.Piller, Handbook of Optical Constants of Solids: Indium Phosphide (InP), (Academic Press, 1985), p.511.

†† linearly interpolated between y=0.0 and y=0.550 compositions.

** calculated using Eg (eV) = $1.35 - 0.72y + 0.12y^2$; x =0.46y from Reference * (above).

decrease the conversion cross-section compared to the non-absorbing case but, as will be shown, the effect of the index step is greater at increasing the nonlinear cross-section.

Several compounds were selected in order to compare the effects of material parameters on calculated nonlinear cross-section. These were Q1.15, Q1.20 and Q1.25 materials. Their relevant material properties are listed in Table 4.2.

4.2.4 Preliminary Design

The initial theoretical design of the waveguide consisted of a multilayer stack alternating between InP and Q-material on an InP substrate. The initial guess for the thickness of each layer was $\lambda/2$, as calculated by,

$$d = \frac{\lambda}{2n_{Re}} \tag{4.8}$$

where λ = 650 nm and n_{Re} was taken from Table 4.2. The $\lambda/2$ thickness calculated for each composition using Eq. (4.8) is also listed in this table. The number of layers of the stack was varied to produce a curve of A_{nl} versus waveguide thickness, as described in Section 4.3.

4.3 COMPUTER ALGORITHM FOR CALCULATING Anl

A computer program was written in the QuickBASIC language to calculate the nonlinear cross-section A_{nl} for a waveguide of known composition and structure. The SEWG operating parameters, including operating wavelength, refractive index information, as well as the desired layer thickness for each composition are used as parametric variables. Given a known number of layers alternating between the two chosen materials, the program calculates the corresponding waveguide mode profile and the value of A_{nl}.

In order to optimize the nonlinear cross-section, an outer loop was added to the program, which allowed iterative changes to be made to the multilayer structure. This permitted the effects of structural thickness on the calculated value of A_{nl} to be observed. The most common method was to vary the thickness of the waveguide by incrementally

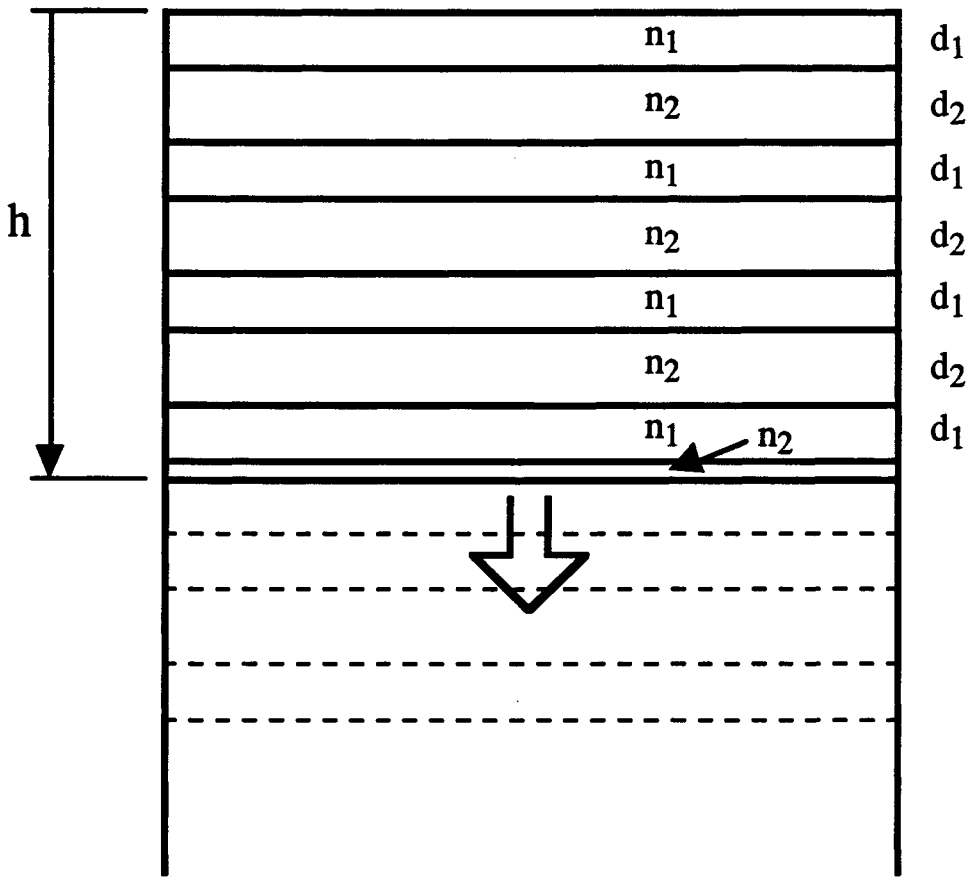

Fig. 4.1: Schematic of multilayer waveguide structure to generate graphs in Fig. 4.2. As the thickness of the waveguide is increased, more layers are added to the bottom of the stack incrementally. When the bottom layer reaches the equivalent of a complete layer thickness (indicated by dashed lines) a new layer of the alternate material is begun.

adding more layers to the bottom of the stack, while maintaining a constant thickness for each layer in the stack, as depicted in Fig.4.1. This meant that the bottom layer would typically be some fraction of a complete layer thickness. When the bottom layer reached the equivalent of a complete layer thickness, a new layer of the alternate material would be started.

4.4 OPTIMIZATION OF SEWG STRUCTURE AND COMPOSITION

Curves of nonlinear cross-section versus waveguide thickness were generated for the three theoretical structures consisting of InP/Q1.15, InP/Q1.20 and InP/Q1.25 multilayers using the algorithm described above. The results of these calculations are displayed in Figure 4.2. The differences between the curves are small on the log plot but the InP/Q1.25 structure clearly possesses the largest nonlinear cross-section. It was thus decided to design the SEWG using an InP/Q1.25 multilayer.

The graphs display some interesting features that require explanation. The most noticeable of these are the resonant peaks in the plots versus thickness. The separation of any two peaks is equivalent to one optical wavelength. The layer thicknesses of the multilayer stack were chosen to be half an optical wavelength using Eq.(4.8), so the peak separation corresponds to the thickness of two layers in the stack. The peaks correspond to an odd whole number of layers in the stack, while the valleys correspond to an even number. This is expected, since in a stack with an even number of layers, all layers can be paired up to produce low net output. If an extra layer is added, it remains unpaired. Hence, the second-harmonic signal from this layer then results in higher net output. The slab waveguide exhibits the same type of behaviour as the multilayer, even though it is uniform in composition. However, if the slab guide is considered to be a multilayer stack with all the layers identical, this result is expected.

For thin structures in the 0.5-0.7 μm range, the slab waveguide provided comparable output with respect to the multilayer. The dominant effect for thin structures is the presence of the extra, unpaired layer in the stack. This result suggests that the arguments presented for using a multilayer are invalid or, alternatively, that the layer thicknesses are unoptimized. However, as the waveguide is made thicker, the output from the slab waveguide drops off rapidly, while the output from the multilayer decreases more

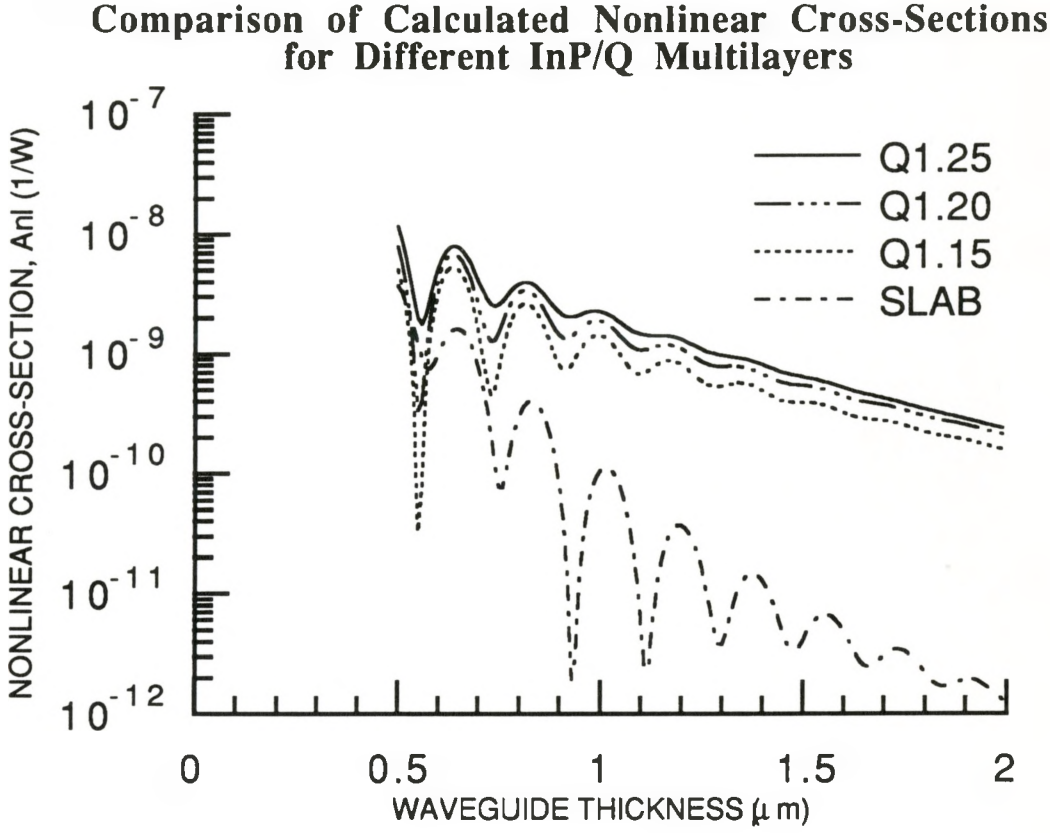

Fig. 4.2: Comparative graph of nonlinear cross-section as a function of waveguide thickness for different multilayers: InP/Q1.25, InP/Q1.20, and InP/Q1.15. Although there are only minor differences between the graphs, the Q1.25 composition clearly produces a larger nonlinear cross-section.

slowly in comparison. This was due to the presence of the multilayer. As more layers are added to the stack, there is a net build-up of output due to non-zero cancellation between the layers. For thicker structures, the multilayer effect dominates device behaviour.

The nonlinear cross-section for a multilayer stack was compared to an identical structure with no material absorption (i.e. the imaginary component of refractive index was arbitrarily set to zero), as shown in Fig.4.3. From this graph it is apparent that the nonlinear cross-section would be significantly higher if the InP/InGaAsP material system were transparent to the harmonic frequency, by as much as 10-100 times. The thicker absorbing structures are significantly worse due to net increased path length as the harmonic signal travels through the waveguide.

Why does the output for the slab waveguide drop off so rapidly? Why would the output from a thick slab structure be so much worse than a thin structure? Wouldn't the extra unpaired "layer" in the stack produce the same net output in both cases? The answers to these questions are two-fold. First, one must realize that the electric field amplitude is not constant throughout the waveguide and is proportional to the square of the electric field mode profile. This means that the nonlinear dipole strength given by Eq.(3.6) varies with thickness throughout the stack, even for a slab waveguide. This results in incomplete cancellation between paired dipoles. Hence, a slab waveguide will produce some net output due simply to the variation in the strength of the radiated harmonic. This variation in dipole strength throughout the waveguide is greater for thin waveguides (where the electric field is confined closer to the surface) than for thick waveguides (where the mode profile is more spread out). Hence, a thin waveguide will tend to have a higher nonlinear cross-section than a thick waveguide.

Second, even though the total optical confinement is higher for a thicker structure, the confinement in the bottom layer of the stack is low. If we think of a slab waveguide as a multilayer, then an unpaired layer on the bottom of the stack will have a much smaller effect on A_{nl} for thicker structures than for thin structures. This unpaired bottom layer provides little contribution to the output. The net result is significantly worse performance. The large material absorption also reduces the conversion cross-section, but the rapid drop-off of A_{nl} occurs even for the non-absorbing case.

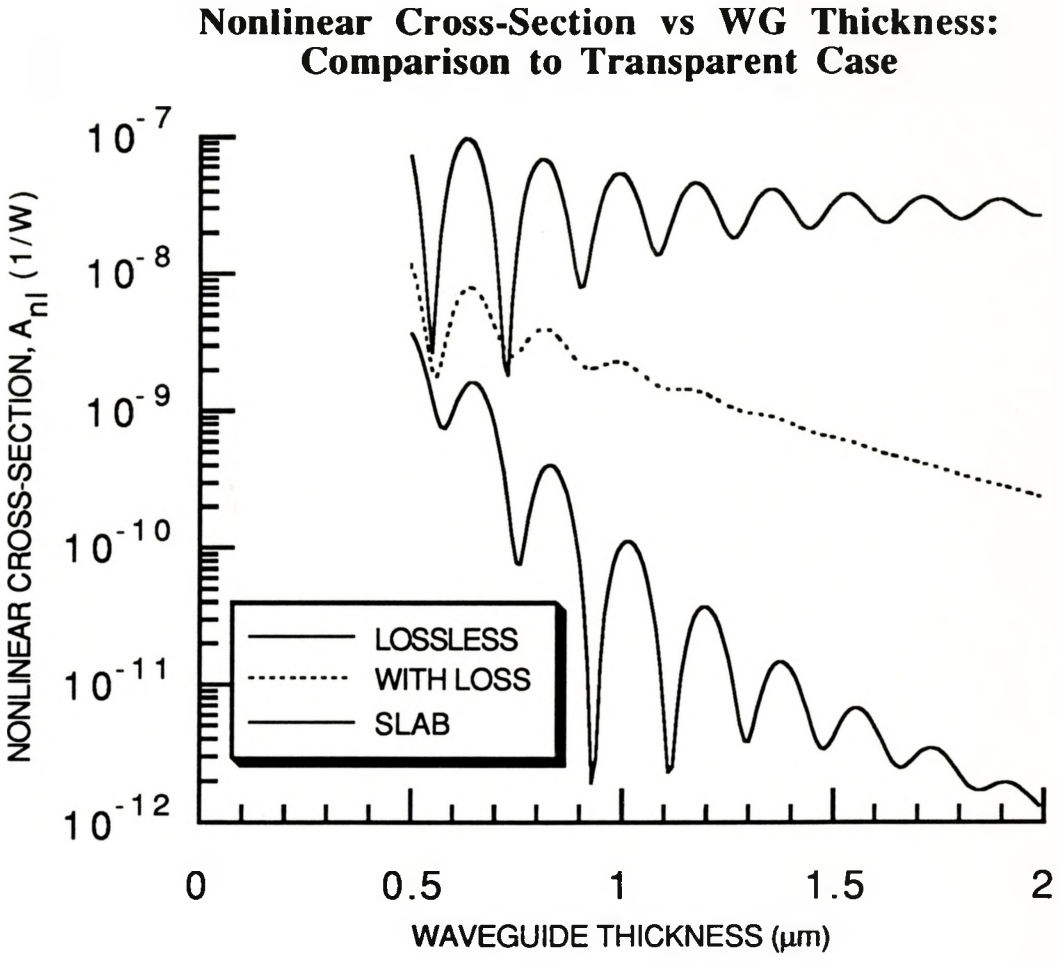

Fig.4.3: Comparison of nonlinear cross-section between a multilayer stack with and without absorption losses. The graph compares the case for the InP/Q1.25 multilayer (from Fig.4.2) to an identical structure (same layer thicknesses and real refractive indices) where the imaginary part of the refractive index has been arbitrarily set to zero.

Another feature of the graphs is the decrease in the depth of the resonant peaks with waveguide thickness. This decrease is more noticeable in the structures with higher absorption, as well (corresponding to larger imaginary refractive index in Table 4.2). As mentioned above, optical confinement is stronger for thicker structures. However, the optical confinement in the bottom layer of the stack will be small. Hence, the effect of the bottom layer has decreasing impact on the device output as the total guide thickness is increased. Also, the second-harmonic signal emitted from this layer has the longest path length to travel before reaching the surface. As material absorption increases, the net output from the bottom of the stack likewise decreases. These effects combine to cause a decrease in modulation depth with thickness, as well as with increasing absorption, as shown in Fig. 4.3.

4.4.1 Number of Layers in Multilayer

The optical output of the multilayer is comparable for thin and thicker structures. However, it is not practical to use a thin waveguide because optical coupling between the waveguide and an optical fiber carrying the fundamental input beam becomes much more difficult due to alignment problems. As well, the coupling efficiency is lower for thinner waveguides, resulting in lower electric field amplitudes in the guided modes and a smaller second-harmonic signal. Hence, a thicker waveguide was desired for the structures.

The total number of layers comprising the multilayer is limited by the number of modes the waveguide will support. The guide should be kept single-mode to produce a single surface-emitted beam. In contrast, a multimode guide would produce a surface-emitted beam for each possible TExTM mode interaction. Single-mode propagation is desired for applications such as high-speed pulsed signal processing, whereas a multimode guide would cause pulse spreading due to modal birefringence. Good mode confinement is desired to ensure that more energy is stored in the multilayer section of the guide rather than the substrate. To improve confinement, an odd number of layers was chosen where the higher index Q1.25 material comprised more of the multilayer than InP. The multimode wavelength cutoff thickness for this guide is ~970 nm. Thus, a 9-layer structure was chosen, with a total guide thickness of ~805 nm. This provided the thickest single-mode guide possessing an odd number of $\lambda/2$ layers.

4.4.2 Optimization of Layer Thickness

Equation 4.8 was used to give an estimate of the $\lambda/2$ thickness for each layer. However, this may not be the optimum thickness for maximizing nonlinear cross-section. Although this choice of layer thickness has improved the cross-section over the slab waveguide case (as demonstrated in Fig. 4.2), it was determined using an approximate case worked out in Section 4.1.1. Confirmation of the choice of a $\lambda/2$ layer thickness is desired.

In order to optimize the layer thickness, the QuickBASIC program was modified to calculate the nonlinear cross-section for a fixed number of layers while varying the thickness of the individual layers. All layers were made the same thickness for simplicity. The optimization routine effectively stretched the multilayer stack to find the thickness with the highest nonlinear cross-section. A schematic of the optimization is shown in Fig. 4.4.

The results for the 9-layer InP/Q1.25 multilayer are shown in Fig 4.5. The peak is at 0.82 μm, corresponding to an individual layer thickness of 91 nm. This thickness is very close to $\lambda/2$, as expected. Note also the broadness of the peak. The width of the peak at full-width half-maximum (FWHM) was 0.2 μm. This corresponds to an allowable error of ±11 nm per layer. The salient feature of the graph is the distinct drop-off of the nonlinear cross-section on either side of the peak. This shows that our intuitive argument for a half-wave stack is correct. Further calculations showed that the nonlinear cross-section is most sensitive to the two-layer period of the multilayer. The cross-section is much less sensitive to exact layer thickness, provided the period remains constant. This justifies making all layers in the stack of equal thickness. (As noted earlier, the model used to generate these curves is only accurate on or near a half-wave stack. The validity of this curve far away from the $\lambda/2$ structure is questionable.)

4.4.3 Waveguide Modal Calculation

The designed waveguide was single-mode where the amplitude of the electric field for the propagating mode is as depicted in Fig. 4.6. The exact solution for the structure is compared to the 3–layer slab waveguide approximation used in the calculations. The mode

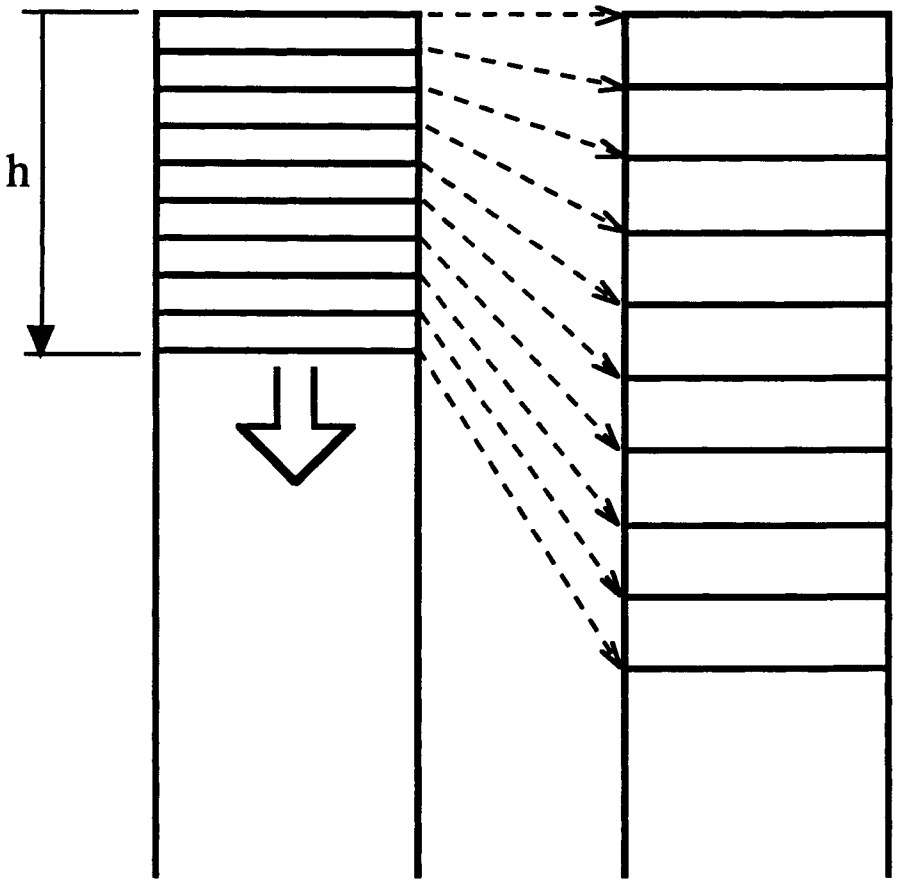

Fig. 4.4: Schematic of waveguide structure used to generate Fig.4.5. As the total thickness h is increased, the thickness of each layer also increases, while the total number of layers remains fixed. This optimizes the layer thickness for some fixed number of layers (in this case, 9).

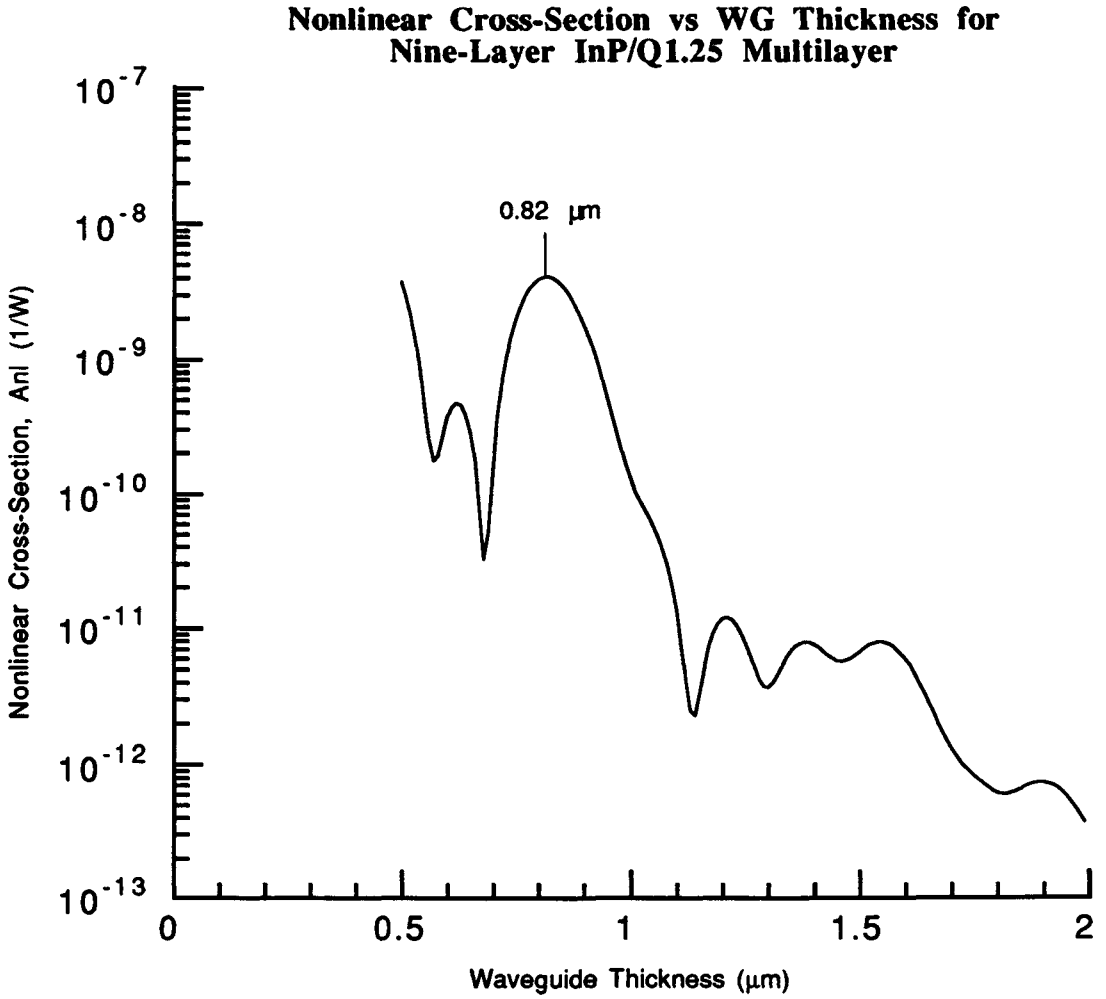

Fig. 4.5: Graph of nonlinear cross-section as a function of waveguide thickness for a 9 layer stack consisting of alternating layers of InP and Q1.25 material. The peak position indicates the optimum thickness for the structure.

profiles for the two cases are very similar, although the exact solution has some minor amplitude variations due to the multilayer. The waveguide effective index for the exact solution is $n_{eff} = 3.257$ as compared to $n_{eff} = 3.299$ for the slab guide. The optical confinement for the exact solution is 90% versus 92% for the slab. The exact modal solutions were calculated with software provided by P.E. Jessop and N.E.J. Hunt.

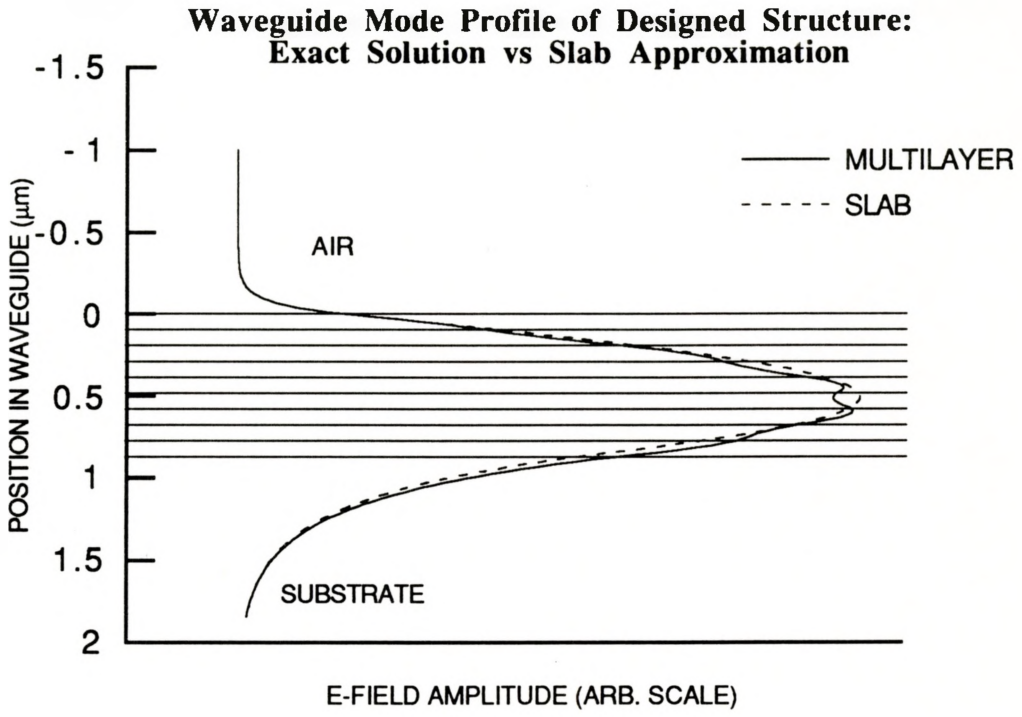

Fig. 4.6: Electric field amplitude of fundamental guided mode for the designed waveguide. The exact calculation for the multilayer guide is compared to the 3-layer slab guide approximation. Exact calculations performed with software provided by N.E.J. Hunt and P.E. Jessop.

CHAPTER 5 - FABRICATION AND CHARACTERIZATION OF DEVICES

5.1 DESIGN SUBMITTED FOR GROWTH

The finalized SEWG design submitted for epitaxial crystal growth is shown in Fig. 5.1. The layer structure is based on calculations made with an earlier model using slightly different refractive index information, resulting in a layer thickness of 94 nm. Note however that the total guide thickness of 0.846 μm is still near the peak of Fig. 4.5.

5.1.1 Doping Effects

The effects of doping on crystal nonlinear coefficient are unknown. It was desired to know if doping could alter the magnitude of the nonlinear susceptibility, allowing the SEWG efficiency to be increased. To explore this, the designed structure was submitted for growth with three different doping profiles. In one, the doping level alternated between 10^{18} cm^{-3} and 10^{16} cm^{-3}. In the second, the doping was reversed. In the third, the doping was kept a constant in all layers at 10^{17} cm^{-3}.

5.1.2 Growth Runs

The SEWG structures were grown using an InGaAsP-based MOCVD machine located in Bell-Northern Research's Advanced Technology Laboratory. Two-inch diameter (100)-oriented InP wafers were used for substrate material. Si was used as the n-type dopant in the samples. Each run was labelled by a run number: R1-621, R1-622 or R1-623. A summary of the submitted growths is presented in Table 5.1. The growths were performed consecutively to minimize any variations in growth composition and rate between samples.

Design of Multilayer SEWG Submitted for Growth

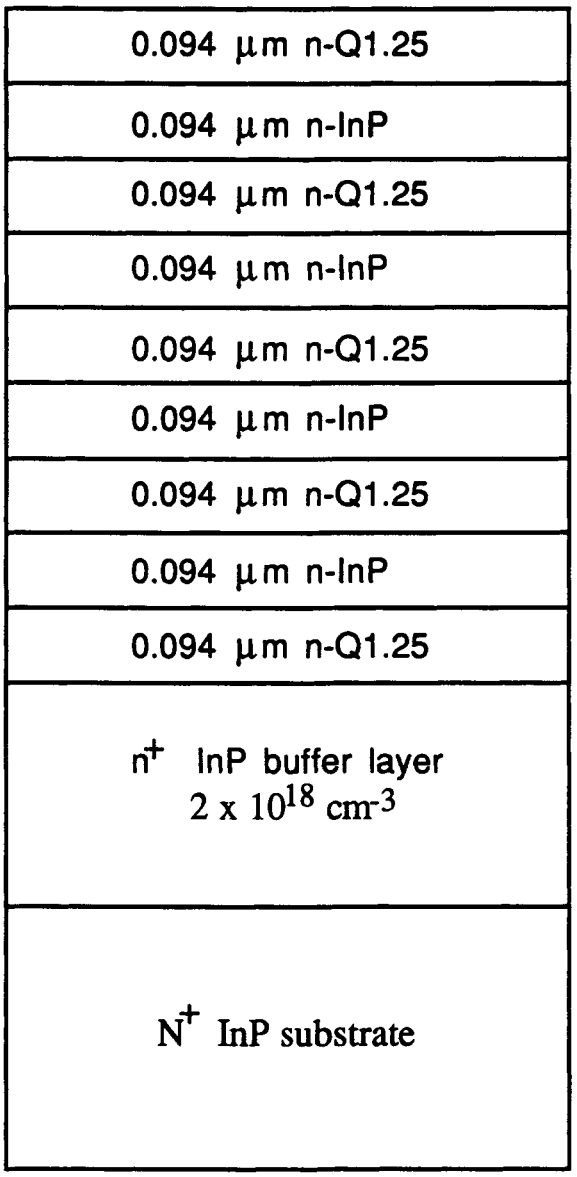

Fig. 5.1: Schematic of the device structure submitted for epitaxial growth, consisting of a nine-layer stack of alternating InP/Q1.25 material and a highly doped buffer layer on an InP substrate.

TABLE 5.1: Summary of Design Parameters for Different SEWG Wafers
(measured parameters after growth shown in brackets)

	Sample Name		
	R1-621	**R1-622**	**R1-623**
	designed (grown)		
Number of layers	9	9	9
InP layer thickness	94 nm (64 nm)	94 nm (102 nm)	94 nm (102 nm)
InP doping level	$1x10^{17}$ cm^{-3} ($\sim 2x10^{17}$ cm^{-3})	$<5x10^{16}$ cm^{-3} ($\sim 5x10^{16}$ cm^{-3})	$1x10^{18}$ cm^{-3} ($\sim 2x10^{18}$ cm^{-3})
InGaAsP layer thickness	94 nm (65 nm)	94 nm (108 nm)	94 nm (108 nm)
InGaAsP doping level	$1x10^{17}$ cm^{-3} ($\sim 5x10^{16}$ cm^{-3})	$1x10^{18}$ cm^{-3} ($\sim 2x10^{18}$ cm^{-3})	$<5x10^{16}$ cm^{-3} ($\sim 4x10^{16}$ cm^{-3})
Buffer doping level	$2x10^{18}$ cm^{-3} ($\sim 2x10^{17}$ cm^{-3})	$2x10^{18}$ cm^{-3} ($\sim 2x10^{18}$ cm^{-3})	$2x10^{18}$ cm^{-3} ($\sim 2x10^{18}$ cm^{-3})
Substrate type	n^+ InP	n^+ InP	n^+ InP

5.2 CHARACTERIZATION

5.2.1 Photoluminescence Data

Photoluminescence (PL) measurements were performed on sample R1-621 after growth. The results indicated that the bandgap wavelength of the quaternary material was approximately 1.23 μm versus the design specified figure of 1.25 μm. The bandgap wavelength varied across the wafers by ±0.013 μm.

5.2.2 SEM Data

A typical scanning electron microscope (SEM) photograph of the samples is shown in Fig. 5.2. Many pictures were taken at several points around the wafer. These revealed that the layer thickness was uniform across the entire wafer. However, the SEM did not have enough resolution to provide accurate measurements of layer thickness. There was an indication that the net thickness of the waveguide was larger than designed.

5.2.3 TEM Data

Transmission electron microscope (TEM) images were taken at BNR for samples R1-621 and R1-623 to get an accurate measurement of layer thickness. An example of these TEM pictures is shown in Fig. 5.3. In both samples, the layer thickness was larger than specified. The quaternary layers were 108nm ± 2nm and the InP layers were 102nm ± 2nm. The thickness of the layers was remarkably consistent from layer to layer and sample to sample. The interface quality was confirmed to be excellent.

5.2.4 SIMS Data

Samples from all three runs were sent for secondary ion mass spectroscopy (SIMS). This technique can be used to measure the concentration of selected elements in a material. A particle beam directed at the wafer surface slowly sputters away the wafer material, which can be monitored with a mass spectrometer to measure the relative concentration of a desired constituent atom of the sample material. By graphing the concentration as a function of time, a concentration profile as a function of depth is made.

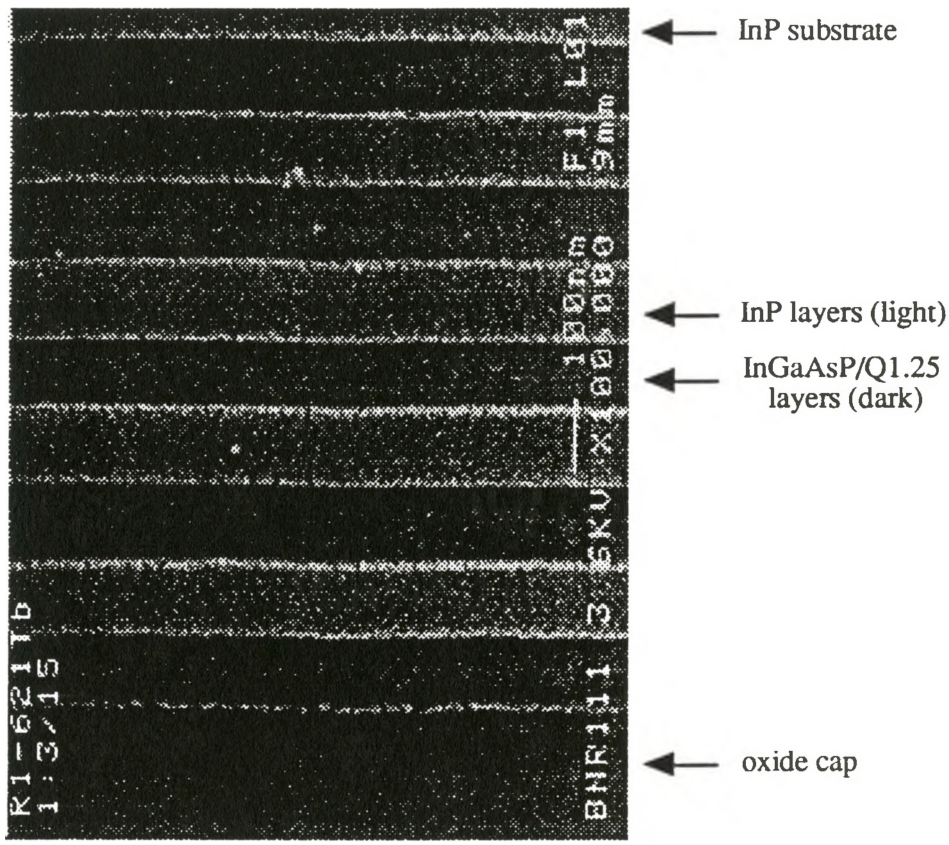

Fig. 5.2: An SEM photograph of the grown multilayer waveguide (sample R1-621). The dark bottom-most layer is the oxide cap that was deposited during processing. Any irregularities along the layer interfaces may be due to a delineation etch that was performed to improve contrast, or may simply be produced artificially by the SEM (caused by external motion affecting the electron beam).

Through careful calibration of sputtering rate and concentration, accurate information of composition and doping level can be extracted.

SIMS analysis was performed on samples from all three growth runs to determine the doping level of Si in the waveguide. The concentration of Ga was also monitored to correlate the doping level with layer composition. The SIMS apparatus was calibrated to measure sputtering rates for pure InP, so the absolute concentration levels of silicon in the quaternary layers were not accurate. The values plotted on the graph were approximately twice the actual level. The SIMS plots are shown in Figs. 5.4 - 5.6 and are summarized in Table 5.1.

The doping levels of Si were close to those specified for the various growths. The most notable deviation was for R1-621, where the doping level of the buffer layer was $1x10^{17}$ cm^{-3} instead of the specified level of $1x10^{18}$ cm^{-3}. The graphs did not reproduce the abrupt changes in concentration in the structure. This is an inherent limitation of the SIMS technique, due to ion intermixing and implantation. Because of this, the measured value of a dip in concentration level may not reflect the true value, before sputtering of an underlying layer begins.

5.3 WAFER PROCESSING

To improve lateral optical confinement, the SEWG was fabricated as a ridge waveguide as well as in slab waveguide form. This was accomplished with an available mask which possessed ridge patterns of various widths.

First, each wafer was coated with a 3000Å SiO_2 mask. Then a photoresist layer was spun on top, followed by a soft baking stage. The wafers were then cleaved into four quarters, labelled a,b,c and d. The 'a' quarter of each wafer was exposed using the ridge mask; the photoresist was then developed and the ridges were etched into the waveguide using a reactive ion etcher. The ridges were etched to a depth of 1.0 μm. The remaining photoresist and oxide were then removed from all four quarters of each wafer. The substrates of the 'a' and 'b' quarters were then thinned to a thickness of ~150 μm using a

lapping and polishing technique, which made cleaving the samples into test bars much easier.

A scanning electron microscope (SEM) photograph of one of the etched ridges is shown in Fig. 5.8, which reveals that the etch left a sidewall slope of ~15°. The top and sidewall surface morphology was smooth, showing no major features to interrupt wave propagation. The ridge depth was measured to be 0.98 μm using an AlphaStep machine. The ridge shown in the picture is 2.0 μm wide.

5.4 COMPARISON WITH DESIGNED STRUCTURE

The TEM data revealed that the layer thicknesses were larger than expected. The total thickness of the guide was 0.948 μm, which would likely make the guide multimode. The waveguide modes for the grown structure were calculated and are graphed in Fig. 5.8, which confirms this prediction.

A curve of A_{nl} versus thickness was generated for a multilayer structure corresponding in material composition and layer thickness to the characterization data for the grown waveguide. The layer thicknesses were 102 nm and 108 nm for the InP and Q1.23 layers respectively. This graph is shown in Fig. 5.9 and is compared to the graph for the designed InP/Q1.25 structure (Fig. 4.4).

Fig. 5.3 : TEM photograph of a multilayer waveguide (sample R1-622).

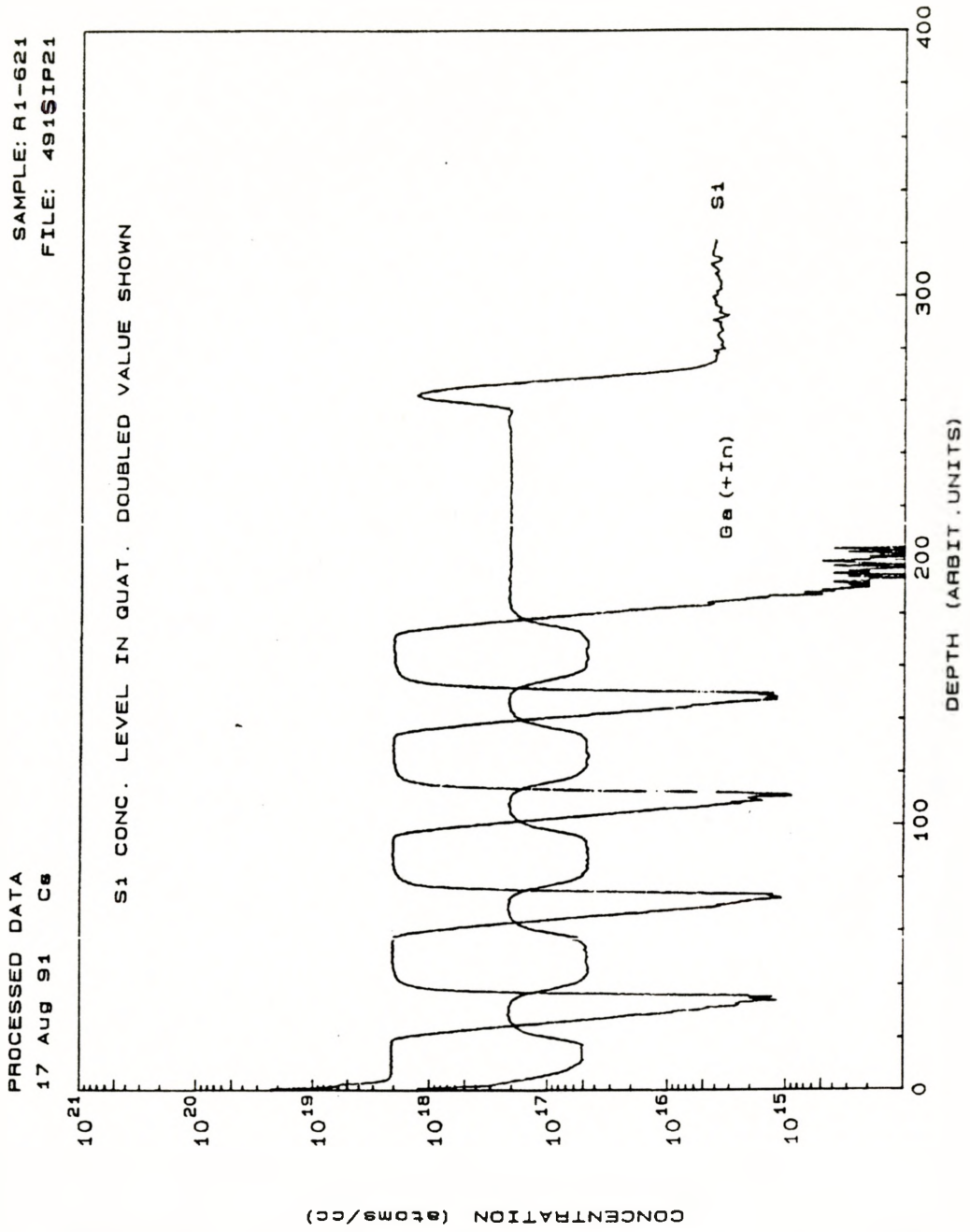

Fig. 5.4: SIMS plot of Si-doping and Ga concentration in sample R1-621 multilayer SEWG. The doping level is approximately constant throughout the stack. Variations are due to uncalibrated measurement in the InGaAsP layers and/or different Si incorporation rates for different compositions during epitaxial growth. The Ga concentration is uncalibrated but its incorporation on the SIMS plots helps delineate the boundaries between the InP and InGaAsP layers.

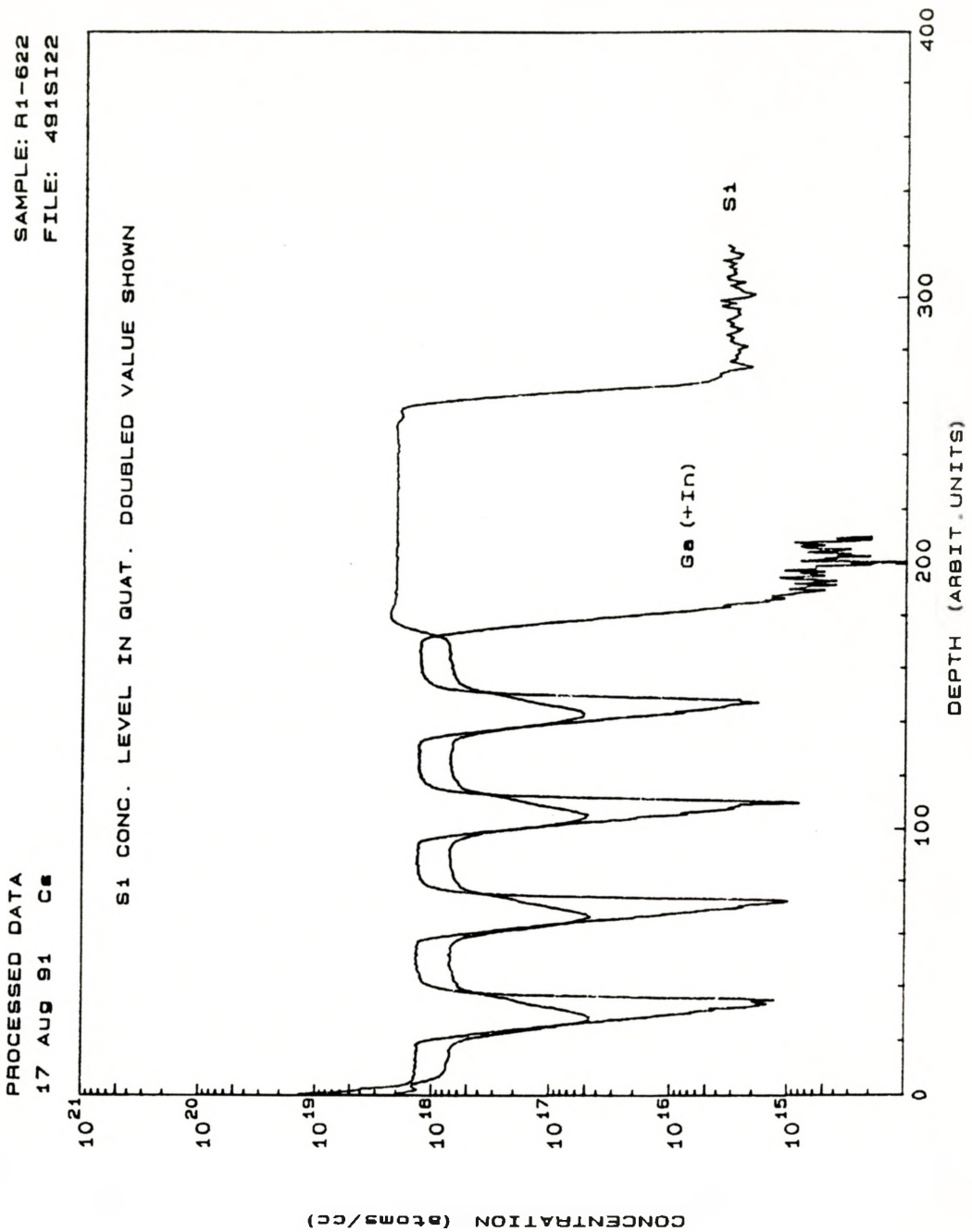

Fig. 5.5: SIMS plot of Si-doping and Ga concentration in sample R1-622 multilayer. The doping level is high in the Q1.25 layers and low in the InP layers, while the substrate is highly doped. The Ga concentration is uncalibrated but its incorporation on the SIMS plots helps delineate the boundaries between the InP and InGaAsP layers.

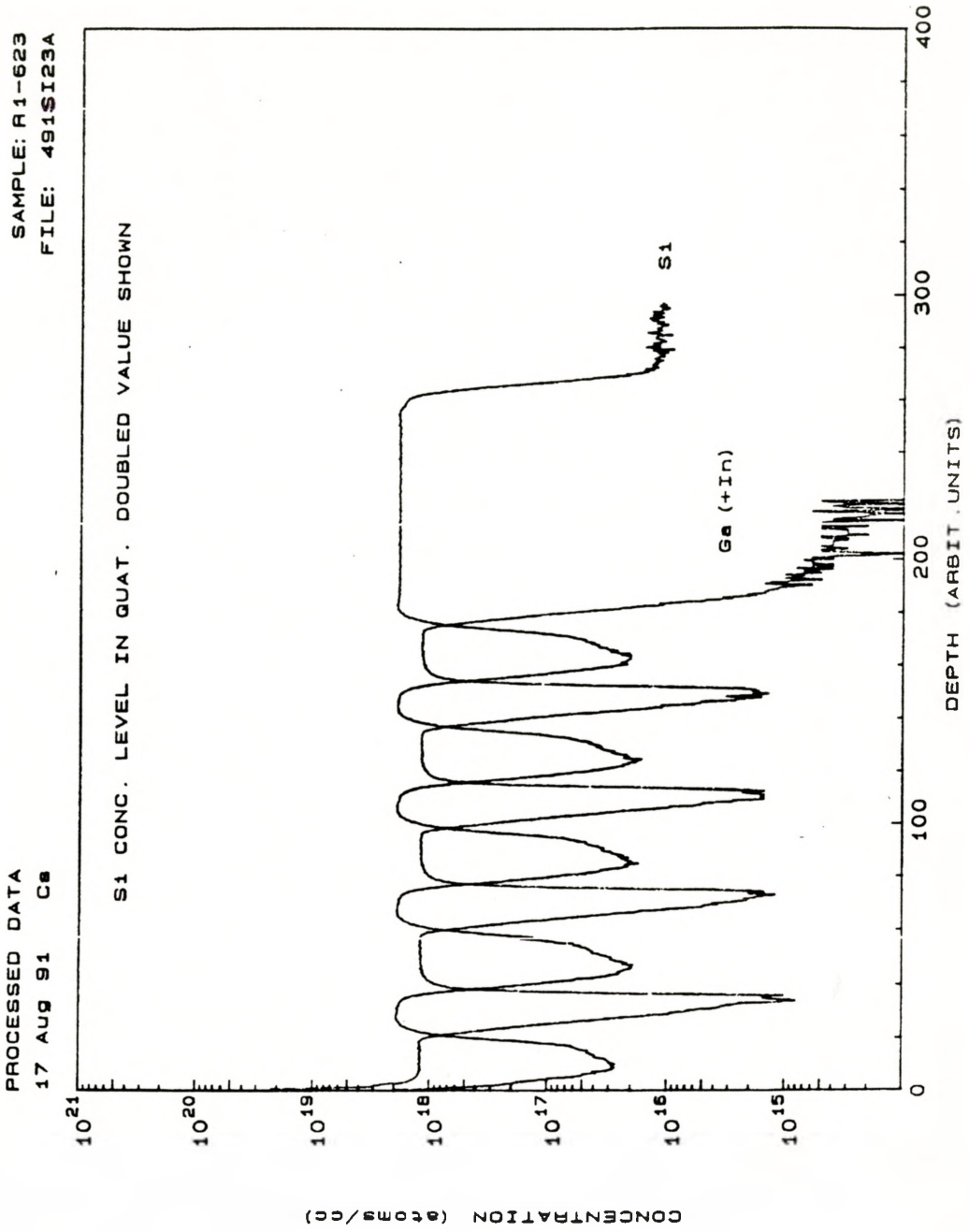

Fig. 5.6: SIMS plot of Si-doping and Ga concentration in sample R1-623 multilayer. The doping level is low in the Q1.25 layers and high in the InP layers, while the substrate is highly doped. The Ga concentration is uncalibrated but its incorporation on the SIMS plots helps delineate the boundaries between the InP and InGaAsP layers.

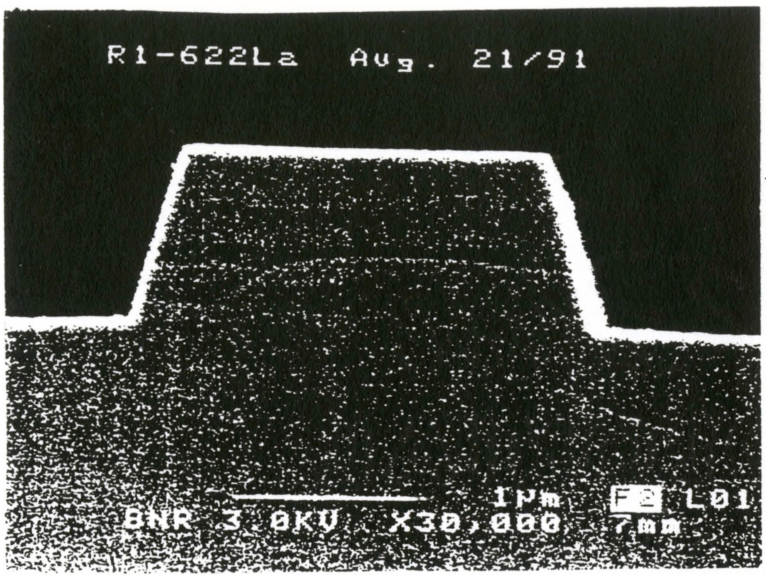

(a)

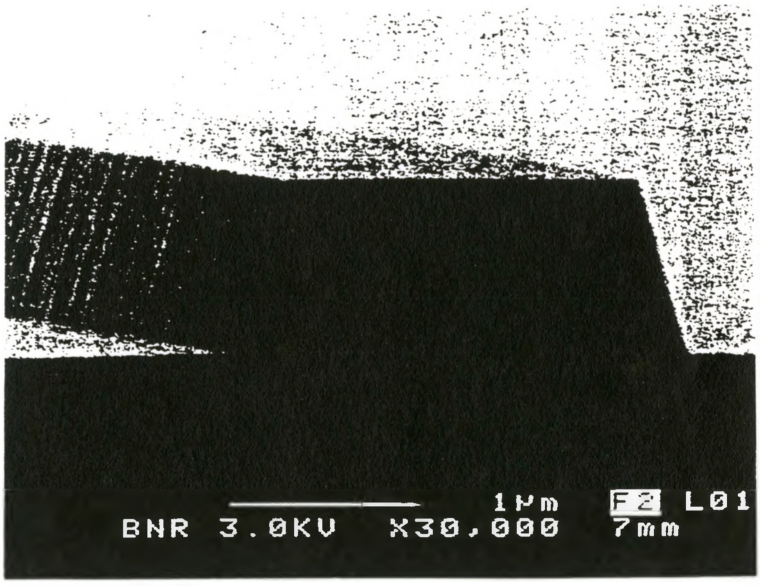

(b)

Fig. 5.7 : SEM photograph of an ridge etched into the multilayer waveguide (sample R1–622) (a) profile view (b) perspective view. The ridge depth is 1 µm; the ridge shown had a width of 2 µm.

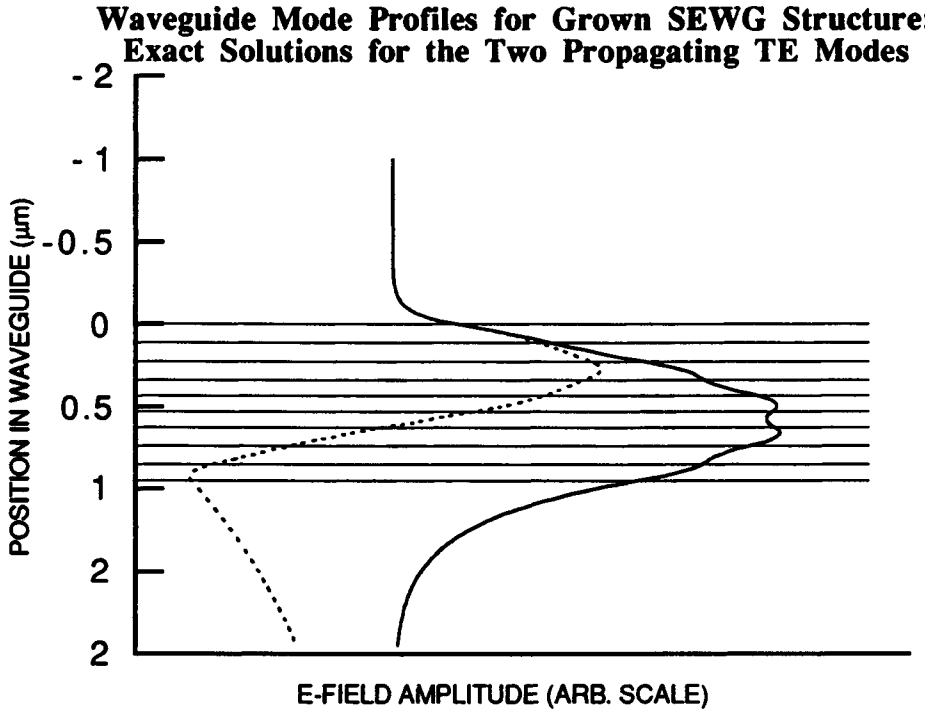

Fig. 5.8: Electric field amplitude for TE-guided modes of the grown waveguide. The waveguide supports the first two TE and TM modes. The exact calculation for the multilayer waveguide is shown for both modes.

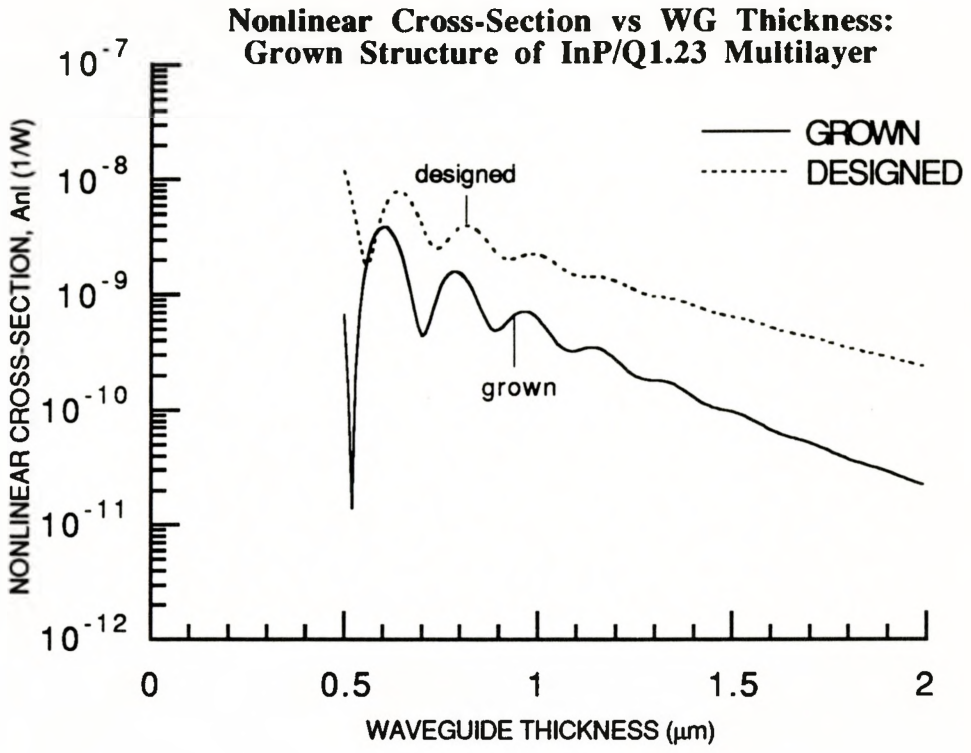

Fig. 5.9: Graph of nonlinear cross-section as a function of thickness for a waveguide of composition and layer thickness corresponding to the grown SEWG. This graph was generated in the same manner as Fig. 4.2 (following the algorithm described in Fig. 4.1) using the layer thicknesses measured from the *single* growth. The predicted nonlinear cross-section for the grown 9-layer structure is indicated on the graph as 7×10^{-10} W^{-1} (versus 4×10^{-9} W^{-1} for the designed structure). The InGaAsP material in the grown sample had an average bandgap wavelength of 1.23 ± 0.013 μm. The thicknesses for the InP/InGaAsP layers were 102 nm and 108 nm respectively (versus a designed layer thickness of 94 nm for both materials).

CHAPTER 6 - EXPERIMENT

This chapter describes the experiment used to analyze the SH radiation and determine the nonlinear cross-section. A discussion of these results is also presented.

6.1 APPARATUS

The experimental apparatus used to image and measure the SH signal consisted of a laser source, an optical fiber, a sample plus a mount, and a CCD camera. A Nd:YAG laser and a semiconductor laser were used as a light source. Both could be operated in pulsed mode and the semiconductor laser could be used CW.

The Q-switched Nd:YAG laser produced pulses with a repetition rate of 10 kHz. The operating wavelength was 1.32 μm. These pulses were 200 ns long and were Gaussian in shape. The average power of the pulses it produced was ~100 mW and was coupled into a single mode fibre having an 8 μm diameter core. The resultant average power out of the fibre was ~10 mW. Coupling efficiency from the fibre to the waveguide was estimated at ~10 %, so ~1 mW average power was launched into the waveguide. The light produced by this laser was unpolarized.

The semiconductor lasers were standard BNR ridged lasers operating around 1.3 μm and produced more than 20 mW CW power. Coupling to the SEWG was achieved through either a single-mode fibre or free-space optics. Fibre-coupling launched almost 10 mW of power into the fibre, which translated to ~1 mW into the guide. The free-space optics used two 40x objective lenses and polarization control elements to couple a similar amount of power into the guide. Alignment to the waveguide was accomplished with the aid of micropositioners. Sometimes, piezocontrollers were also used to increase the alignment precision to <0.1 μm.

The surface-emitted signal was measured and imaged with a Silicon CCD camera that was thermoelectrically cooled to -40°C to improve resolution. A computer attached to the CCD array processed the information received from the camera. This was used to image the surface emission, as well as to determine the total amount of power incident on the array. The array itself was composed of 575 x 383 pixels. Each pixel was 23 μm x 23 μm in size. The total size of the array was 13.2 mm x 8.8 mm, which corresponded to the dimensions of the pictures shown in Figs. 3.4 and 6.1.

6.2 COUPLING TO THE SEWG

6.2.1 TE and TM Mode Polarization

Second-harmonic generation in the SEWG required that two counter-propagating modes interact, where one mode was TM and the other TE. Experimentally, it was much simpler to couple one beam into the waveguide (slab or ridge). The second counter-propagating beam would be supplied by the back-reflection from the far-facet, which had a reflection coefficient of R=0.3. However, if the first mode is TE^+ then the reflected mode will be TE^-, resulting in no surface emission at all. To avoid this problem, both the TE^+ and TM^+ were launched when coupling light into the waveguide. The reflected beam would then provide two interactions, consisting of $TE^+ \times TM^-$ and $TM^+ \times TE^-$. The angle of surface emission from these two interactions would also be the same. However, they would be on different sides of the surface normal and would appear as mirror images.

To maximize the power of the SH radiation, the power in the two modes should be made equal. This meant coupling equal amounts of light into the TE and TM modes from the optical fibre (or lens). Control of the polarization was straightforward with the Nd:YAG laser since the output was unpolarized. Hence, similar powers were automatically coupled into the modes. With the semiconductor laser, the polarization of the light entering the waveguide was adjusted so that the power of the beam exiting the far facet of the guide was split equally between TE and TM.

6.2.2 Optical Alignment to the Waveguide

The SEWG was operated in both slab and ridge waveguide configurations. Alignment of the optical fibre to the ridge was more difficult, since the fibre had to be accurately positioned both vertically and laterally. Furthermore, the coupling efficiency was expected to be slightly less, since the ridge width of 6.6 μm was slightly narrower than the fibre core diameter. However, the ridge provided lateral confinement for the optical beam whereas the slab did not. This caused several problems when using a slab waveguide. First, the optical beam had to be aligned normal to the cleaved facets. This ensured that the beam and its reflection from the far facet were propagating in opposite directions in the waveguide. Second, the beam spread out as it propagated along the length of the guide. However, experimental measurements indicated that the beam divergence was negligible, even after propagating a length of 1 mm in the guide. This was attributed to the high refractive index of the semiconductor material, as compared to the fibre. The high refractive index tended to collimate the beam.

Another effect to consider was multiple reflections in the guide. The cleaved facets at the ends of the waveguide could act as a high-loss Fabry-Perot cavity. With a mirror reflectivity of R=0.3, the cavity intensity would build up to be as much as 1.4x the input intensity and would tend to increase the second-harmonic signal.

6.3 SURFACE IMAGING

6.3.1 Near-Field Image

The SH signal emitted from the SEWG was focused onto the CCD array with the aid of a 50 mm focal length lens. An image of the surface emission taken by the CCD camera is shown in Fig. 3.4. The streak running across the length of the 0.5 mm wide sample is the second-harmonic signal. The beaded appearance of the streak is due to the beating of the TE and TM standing waves, as described in Section 3.4. The beating has a spatial period of ~100 μm.

6.3.2 Fourier Transform Image

The analysis presented in Chapter 5 revealed that the grown SEWG waveguide was multimode. The waveguide supported 4 modes, which included the 0^{th} and 1^{st} order TE and TM modes. These will be labeled $TE_{0,1}$ and $TM_{0,1}$. All four modes propagate in both directions due to the back-reflection.

The presence of the higher-order modes in the waveguide resulted in the occurrence of several interactions in addition to the predicted TE_0 x TM_0 interaction used in the modeling. Other allowable interactions that would produce a surface-emitted beam were TE_0 x TM_1, TE_1 x TM_0, and TE_1 x TM_1. Each of these interactions results in surface emission at a different angle, as determined by the difference in propagation constants, $\Delta\beta$, for the particular modes involved.

Figure 6.1 shows a Fourier transform image of the surface-emitted beam. This was produced by placing the CCD array at the focal plane of the lens used to collect the SH radiation. Eight lines appear on the photograph, corresponding to the four predicted modal interactions and their mirror images. This picture confirmed the presence of multiple modes in the waveguide. The interactions that produced the different emission lines could be deduced from a knowledge of the modal propagation constants. The 2 innermost faint lines are caused by the TE_0 x TM_0 interaction, since the propagation constants of these two modes are closest together. Moving outward, the next two lines are due to the TE_1 x TM_1 interaction. The outermost sets of lines are caused by the TE_1 x TM_0 and TE_0 x TM_1 interactions respectively.

The modal propagation constants were calculated for the waveguide. From these, the emission angles were calculated. These were compared to the emission angles measured using Fig.6.1. The results of these findings are listed in Table 6.1. Good agreement was found between theory and experiment. The largest source of error was uncertainty in the refractive index, as a result of the high doping level. The resolution of the device was also calculated, based on the width of the lines shown in Fig. 6.1. If signals at different wavelengths are mixed in a single-mode guide, the SEWG is capable of resolving wavelength differences of less than 2 nm, as a conservative estimate. This value assumed negligible modal dispersion, as would be the case in a pure TE x TE interaction.

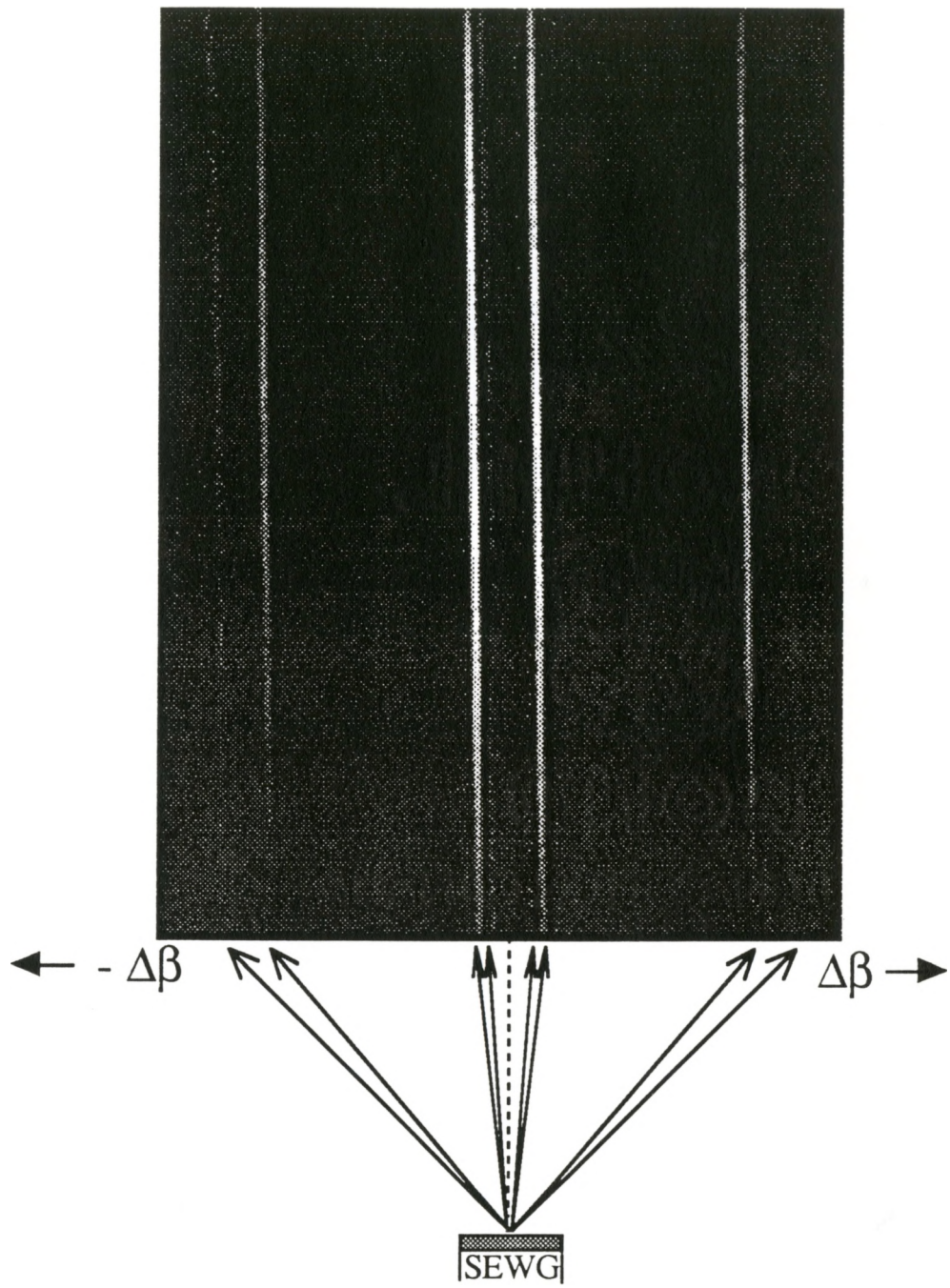

Fig. 6.1: Far-field surface emission pattern of second-harmonic signal. This image demonstrates the different surface emission angles, as determined by momentum conservation. This waveguide supports 4 different optical modes (TE_0, TM_0, TE_1, TM_1), resulting in a total of 8 emission lines. (The actual emission angles have been greatly exaggerated in the schematic.)

Table 6.1: Propagation Constants and Surface Emission Angles of Different TE x TM Interactions from the SEWG

(a)

MODE	EFFECTIVE INDEX
TE_0	3.314
TM_0	3.309
TE_1	3.215
TM_1	3.210

(b)

INTERACTION	EMISSION ANGLE (degrees) CALCULATED	MEASURED	$\Delta\theta$
$TE_0 \times TM_0$	0.13°	0.19°	0.06°
$TE_0 \times TM_1$	2.97°	3.08°	0.11°
$TE_1 \times TM_0$	2.69°	2.62°	-0.07°
$TE_1 \times TM_1$	0.15°	0.24°	0.09°

The effective index information was calculated using software provided by P.E. Jessop and N.E.J. Hunt. The solutions are for the exact 11-layer waveguide (9 guide layers plus air and substrate), not for the slab waveguide approximation.

This figure-of-merit would improve with higher nonlinear cross-section (and hence higher second-harmonic power), a longer waveguide, shorter camera exposure time, and better vibration isolation. These refinements would help attain the 1 Å resolution predicted in Ref. [8].

The SHG radiation is effectively a plane wave emitted from the waveguide surface. Each interaction produces a plane wave at a different emission angle. The plane waves are finite in extent, limited by the length and width of the interaction area inside the waveguide. The angle of emission along the direction of propagation (z-direction) is fixed by momentum conservation requirements. However, there is no such restriction in the lateral direction (y-direction) across the waveguide. Therefore, the SHG radiation can spread in this direction due to diffraction out of the top surface. By focusing the SHG radiation with a lens, lines are formed due to this lateral spreading instead of a single spot, as would be expected from a collimated plane wave. The amount of this spreading is determined by the beam width, due to refraction. The total dispersion angle was ±2° for the slab guide and ±4° for the ridge. The image in Fig. 6.1 is simply a Fourier transform of the near-field image shown in Fig. 3.4.

Returning to the near-field image, there should be four sets of standing waves inside the waveguide, one for each of the allowed waveguide modes. Hence, the near-field image shown in Fig. 3.4 is the product of the beating of several standing waves, not just one. This explained the very short beat period of the emission pattern. Other emission patterns observed using single-mode GaAs-based guides exhibited longer beat lengths (for example, see Ref. [8]).

6.4 SECOND-HARMONIC POWER AND NONLINEAR CROSS-SECTION

The CCD camera was used to determine the average power of the surface-emitted radiation. This information was taken from the near-field image (Fig. 3.4) by finding the total energy accumulated by the CCD array. The average power was calculated with a knowledge of the exposure time. This was done for both ridge and slab waveguide configurations.

The average power emitted from the ridge was 8.0×10^{-14} W; from the slab, the power was 1.2×10^{-14} W with an error of ±20%. The waveguide samples used for the measurements were 0.5 mm long. The fundamental beam width in the slab guide was approximately 10 μm.

6.4.1 Calculation of Nonlinear Cross-Section A_{nl}

The value of the nonlinear cross-section was calculated using Eq.(3.42). In order to properly compare the measured value of A_{nl} with the theoretical calculations of Ch. 4, several factors must be taken into account. First, the measurements were taken using the pulsed Nd:YAG laser source. Since the process of SHG is nonlinear, a single pulse from the laser produces much more SH intensity than a CW time-averaged signal spread over one period of the laser's duty cycle. The measurement of the surface-emitted radiation was a time-averaged measurement and did not take the pulsed nature of the SH signal into account. If the nonlinear cross-section is calculated using the averaged powers for the fundamental and harmonic beams, the resulting value will be larger than expected. To correct for this, the measured value of A_{nl} must be divided by the duty cycle of the laser (~500).

For the theoretical calculations in Chapters 3-5, the device dimensions were chosen to be l =10 mm long by w=1 mm wide. Equation (3.51) shows that A_{nl} scales as the aspect ratio l /w. For all the theoretical calculations, this aspect ratio was 10. (Interestingly, the nonlinear cross-section does not depend on the absolute surface dimensions of the device.) However, the cleaved bar used in the measurements was only 0.5 mm across with a 10 μm beam width (6.6 μm for the ridge), so the actual aspect ratio of the guide was 50 (75). In order to compare the measured value of A_{nl} with the calculated value, the measured value must be scaled to correspond to a guide with an aspect ratio of 10. This means dividing the measured value by the difference of 5 (7.5).

The total input beam power was estimated to be 1 mW. This was divided equally between TE^+ and TM^+ modes, since the source was unpolarized. However, the guide itself was multimode. This made it impossible to accurately predict the coupling efficiency to the different order modes. Also, the theoretical predictions for the nonlinear cross-

section were made for a single-mode guide only. Hence, the measured value of A_{nl} was computed as if the guide were truly single-mode.

The mirror facet reflectivity was R = 0.3, so the counter-propagating beam intensities of the reflected TE^- and TM^- modes were both 0.15 mW. This resulted in two surface-emitting interactions, $TE^+ \times TM^-$ and $TM^+ \times TE^-$. Each of these interactions produced SH signals of similar intensity, since the power product of the fundamental beams was the same, according to Eq. (3.51). In other words, each of these interactions produced only half of the second-harmonic power quoted above.

Taking the above factors into account and substituting them into Eq. (3.42) yields an experimental value of $A_{nl} = 1.4 \times 10^{-10}\ W^{-1}$ for a ridged sample and $3.2 \times 10^{-11}\ W^{-1}$ for a slab waveguide. The predicted value for the grown structure was $7 \times 10^{-10}\ W^{-1}$ (taken from Fig. 5.9).

6.4.1 Sources of Error

Although there were numerous sources of error, in the end, the agreement between the experimental and predicted values of nonlinear cross-section was reasonable. The most obvious source of error was that the guide was multimode. The cross-sections for the extra, allowed multimode interactions were not taken into consideration in the theoretical calculation. Also, the value of nonlinear susceptibility d_{14} and its dispersion with material was poorly known, adding uncertainty to the predicted value.

The uncertainty in the fundamental optical power launched into the waveguide was another source of error. The power of the Nd:YAG laser source was unsteady during operation, often losing as much as 50% of its peak power. The power in the guide depended critically on the optical alignment of the laser to the fibre and the fibre to the guide. Other errors associated with the collection of the surface-emitted radiation included light scattering off the collecting lens, incomplete light collection, and surface scattering due to contamination of the waveguide surface.

There was also a large difference in the SH powers and nonlinear cross-sections between the ridge and slab cases. This was mainly due to the lateral confinement provided

by the ridge. The overlap of the waveguide mode with its reflection was exact in the ridge, while in the slab it was subject to alignment errors. The second-harmonic signal will only be produced in places where the two counter-propagating modes are overlapping in the guide; if the beams are misaligned, no signal is produced. Also, the ridge and slab measurements were subject to variations in the modal power, as described above. Considering the discrepancy between these two cases, which were from exactly the same sample, it was notable that the predicted value agreed so well.

CHAPTER 7 - CONCLUSION

In this work, the SEWG device has been successfully modeled and implemented in the InP-InGaAsP material system for the first time. Near-field and far-field surface-emission patterns confirmed the predicted nature of the nonlinear mixing process. The measured emission angles of the SH radiation agreed well with theoretical predictions. The measured nonlinear cross-section of the grown device was measured to be 1.4×10^{-10} W^{-1} from a ridged sample and 3.2×10^{-11} W^{-1} from a slab sample.

Due to a lower nonlinear cross-section, the InP-InGaAsP system proved to be inferior to the GaAs-AlGaAs system for implementing the SEWG device. The reason for this was the strong material absorption of the harmonic signal in the InP-InGaAsP material at the operating wavelength chosen. In contrast, a completely transparent device can be grown in the GaAs-AlGaAs system, resulting in a 10- to 100-fold increase in the nonlinear cross-section (when considering only absorption effects). To eliminate the absorption problem, longer operating wavelengths are desired. Wavelengths on the order of 2 μm are necessary to achieve transparency, which does not fall near the silica fibre windows of 1.3 and 1.55 μm.

Alternatively, larger bandgap material that is also lattice-matched to InP could be used, such as InAlAs. Monolithic integration is still possible, since this material is becoming a common choice of material for newer HBT and FET devices. However, most linear, optically active devices (such as lasers, modulators and detectors) that are designed for use in long-distance fiber-optic telecommunications will have bandgap wavelengths near 1.3 or 1.55 μm, so they will be optically absorbing at the harmonic wavelengths (650 and 775 nm). On the other hand, if short-distance communications wavelengths are desired, GaAs-based technology can be used. The SEWG is therefore fundamentally incompatible with other device structures that are designed to operate at the fundamental wavelength of the SEWG.

The layer thicknesses of the grown multilayer waveguide deviated significantly from the design specifications, resulting in a multimode waveguide with unoptimized nonlinear cross-section. It is possible to regrow the SEWG to match the designed layer thicknesses more closely, producing a single-mode guide with a higher predicted nonlinear cross-section. Although a confirmation of the theoretical calculations might be gained, such knowledge would not help attain the original goals of this work - to design and implement the SEWG device in the InP-InGaAsP system. Furthermore, the regrowth would represent only marginal improvements in performance, while using up valuable resources and man-power. Hence, it was felt that such a regrowth was unwarranted.

7.1 MODELING

A working model of the SEWG has been presented in this work which is capable of adequately explaining the behaviour of the device. It is also capable of predicting the nonlinear cross-section for a limited type of waveguide structure, including waveguides composed of a multilayer stack that was on or near a half-wave stack. The limitation on the range of structures for which the modeling is valid results from ignoring the multiple interface reflections inside the stack. However, calculations show that this effect is small, due to the small reflection coefficients at the boundaries. The partial optimization that was performed in this work indicated that a half-wave stack produces the largest nonlinear cross-section of any multilayer stack composed of any two given materials.

A reliable prediction for the nonlinear cross-section of the *grown* SEWG device was not calculated, due to limitations in the complexity of the computer algorithm written to calculate A_{nl}. The waveguide was designed to be single-mode in order to limit the complexity of the modal mixing in the device to the $TE_O x TM_O$ interaction only. However, the grown waveguide was thicker than expected, resulting in a multimode guide. The computer algorithm is unable to calculate the nonlinear cross-section for these higher order modes. Also, it is extremely difficult to predict the optical coupling efficiencies of the input beam to the different modes, making it impossible to accurately find the nonlinear cross-sections of the grown guide (for the various interactions), even if there was a theoretical calculation for comparison. (These are the same reasons a single-mode guide is desirable!) Although the multimodality of the guide made it impossible to

confirm the accuracy of the theoretical calculations, it did allow confirmation of the modal mixing process, as observed in the far-field radiation pattern (Fig. 6.1).

7.2 FUTURE WORK

A more accurate model of the SEWG is desired, such as was recently published by Vakhshoori [29]. This model treats the waveguide as an optically active multilayer stack with complex reflection coefficients at all boundaries in the multilayer. It takes into account multiple reflections in the stack and the effects of the downward-propagating beam. Implementation of such a model will allow more accurate and thorough optimization of the SEWG. However, further work in the InP material system is not warranted unless a significant breakthrough is achieved that will make it competitive with GaAs. Unless this happens, GaAs-AlGaAs is the material of choice for device operation.

In order to make the SEWG a truly useful device for telecommunications, the nonlinear cross-section must be improved dramatically. Efficiencies on the order of 1% or higher would be necessary to reach this level of viability. The most important requirement for future device optimization is a knowledge of the material optical nonlinearity $\chi^{(2)}$. Measurements of nonlinearity versus material composition are vital to accurate device modeling.

There are also several design changes that can be implemented to improve the SEWG. For example, it has been suggested [4] that use be made of the downward-propagating wave that is lost to the substrate by installing a buried optical reflector below the waveguide. This has the potential of doubling the second-harmonic output, although an initial estimate of 20% improvement [29] may be more realistic. The waveguide can also be grown [4, 29] on a (111)- or (110)-oriented substrate, with improvements in nonlinear cross-section by factors of 4/3 and 8/3 respectively over the (100) case. This also eliminates the need for both TE and TM modes in the guide, which simplifies optical coupling.

It is also possible to integrate the SEWG structure with a laser [4, 33]. The internal intensity of the laser can be extremely high, especially if high-reflectivity coatings are placed on the facets. Vakhshoori [8] predicts second-harmonic powers as

high as 0.25 mW of coherent green light for a guide fundamental power of 100 mW. More difficult to achieve are the ideas that suggest [33, 29] elimination or inversion of the material nonlinearity in alternating layers in the multilayer waveguide. A domain-inversion would produce the phase-matching criterion required for truly efficient SHG. Vakhshoori [29] predicts second-harmonic powers of over 4 mW for a SEWG structure with domain-inversion layers that is integrated with a laser and having an internal laser power of 200 mW.

The nonlinear second-harmonic generation process upon which the SEWG is based is a second-order effect. This means that it is inherently small unless very high intensities are used. Reasonable second-harmonic powers are predicted only when the SEWG design is integrated with a laser. However, the sub-milliwatt power levels commonly used in fibre-optic communications lie far below the internal cavity intensities of a laser. For the case of the domain-inversion example above, an input power of 1 mW would produce a second-harmonic power on the order of 0.1 μW. The question to be asked is whether this power level is sufficient for megabit and gigabit data rates. However, these are certainly acceptable power levels for several other applications such as wavemeters, spectrometers and signal processors.

There are still several interesting engineering problems that must be solved to produce the efficiencies desired for SEWG operation. If this can be done, then the SEWG device has exciting potential in many applications.

REFERENCES

1. P. A. Franken, A. E. Hill, C. W. Peters, G. Weinreich, "Generation of Optical Harmonics", *Phys. Rev. Lett.* 7 (4), 118 (1961).

2. A. Yariv, Quantum Electronics, 3ed. New York : Wiley, 1989, p.387.

3. P. J. Vella, R. Normandin, G. I. Stegeman "Enhanced second-harmonic generation by counter-propagating guided optical waves", *Appl. Phys. Lett.* 38 (10), 759 (1981).

4. R. Normandin, R. L. Williams, F. Chatenoud, "Enhanced Surface Emitting Waveguides for Visible, Monolithic Semiconductor Laser Sources", *Electron. Lett.* **26** (25), 2088 (1990).

5. R. Normandin, G. I. Stegeman, "Nondegenerate Four-Wave Mixing in Integrated Optics", *Optics Letters* **4** (2), 58 (1979).

6. D. Vakhshoori, S. Wang, "Demonstration of an AlGaAs/GaAs Integrable Optical Correlator Using Surface-Emitting Second-Harmonic Generation", *Appl. Phys Lett.* **53** (5), 347 (1988).

7. R. Normandin, G. I. Stegeman, "Picosecond Signal Processing with Planar, Nonlinear Integrated Optics", *Appl. Phys Lett.* **36** (4), 253 (1980).

8. D. Vakhshoori, "Integrable Semiconductor Optical Correlator, Parametric Spectrometer for Communication Systems", *J. Light. Tech.* **9** (7), 906 (1991).

9. H. R. Philipp, H. Ehrenreich, "Optical Properties of Semiconductors", *Physical Review*, 129, 1550 (1963).

10. A. Yariv, Optical Electronics 3ed. New York: Holt, Rinehart and Winston, 1985, p. 128.

11. Y. R. Shen, The Principles of Nonlinear Optics (J. Wiley and Sons) 1984, Ch. 10.

12. S. Bhagavantam, Crystal Symmetry and Physical Properties 1966, p. 72.

13. N. Bloembergen, Nonlinear Optics New York: Benjamin, 1965.

14. J. A. Armstrong et al, *Physical Review* 127, 1918 (1962).

15. D. A. Kleinman, "Nonlinear Dielectric Polarization in Optical Media", *Physical Review* 126, 1977 (1962).

16. S. Bhagavantam, Crystal Symmetry and Physical Properties 1966, pp.38-39.

17. "Standards on Piezoelectric Crystals", *Proc. IRE* 37, 1378 (1949).

18. R. C. Miller, "Optical Second Harmonic Generation in Piezoelectric Crystals" *Appl. Phys. Lett* 5 17 (1964).

19. P.G. Harper, B.S. Wherret Nonlinear Optics Academic, 1975, p. 28.

20. A. Yariv, Optical Electronics 3ed. New York: Holt, Rinehart and Winston, 1985, pp. 229-233.

21. S. Jha and N. Bloembergen, "Nonlinear Optical Susceptibilities in Group-IV and III-V Semiconductors", *Physical Review* 171 891 (1968).

22. C. Flytzanis, J. Ducuing, *Physical Review* 178 1218 (1969).

23. C. Flytzanis, J. Ducuing, "Second Order Optical Susceptibility of III-V Compounds", *Physics Letters* 26A 315 (1968).

24. B. F. Levine, "Bond-Charge Calculation of Nonlinear Optical Susceptibilities for Various Crystal Structures", *Phys. Rev. B* 7 2600 (1973).

25. M. M. Choy, S. Ciraci, R. L. Byer, "Bond-Orbital Model for Second-Order Susceptibilities", *IEEE J. Quant. Elec.* QE-11 40 (1975).

26. C. L. Tang, C. Flytzanis, *Phys. Rev. B* 4 2520 (1971).

27. P.G. Harper, B.S. Wherret Nonlinear Optics Academic, 1975, Ch. 1.

28. N. Ogasawara "Second Harmonic Generation in an AlGaAs DH Laser", *Japn. J. Appl. Phys.* **26,** 1386 (1987).

29. D. Vakhshoori, "Analysis of visible surface-emitting second harmonic generators", *J. Appl. Phys.* **70** (10),5205 (1991).

30. A. Yariv, Quantum Electronics, 2nd Ed. (J. Wiley & Sons, New York) 1975.

31. E. Hecht, Optics, 2nd Ed. (Addison-Wesley) 1987.

32. J.A. Armstrong, N. Bloembergen, J. Ducuing, P.S. Pershan, "Interaction between light waves in a nonlinear dielectric", *Phys, Rev.* 127, 1918 (1962).

33. R. Normandin, S. Létourneau, F. Chatenoud, R.L. Williams, "Monolithic, Surface-Emitting, Semiconductor Visible Lasers and Spectrometers for WDM Fiber Communication Systems", *IEEE J. Quant. Electr.* **27** (6), 1520 (1991).